

See discussions, stats, and author profiles for this publication at: <http://www.researchgate.net/publication/256860063>

Unraveling the geometry of the Farallon Plate: Synthesis of three-dimensional imaging results from the USArray

ARTICLE *in* TECTONOPHYSICS · APRIL 2012

Impact Factor: 2.87 · DOI: 10.1016/j.tecto.2012.02.008

CITATIONS

28

READS

59

5 AUTHORS, INCLUDING:



[Gary Pavlis](#)

Indiana University Bloomington

118 PUBLICATIONS **1,265** CITATIONS

SEE PROFILE



[Karin Sigloch](#)

University of Oxford

74 PUBLICATIONS **486** CITATIONS

SEE PROFILE



[Matthew J. Fouch](#)

k. young consulting

146 PUBLICATIONS **2,468** CITATIONS

SEE PROFILE



[Frank L. Vernon](#)

University of California, San Diego

240 PUBLICATIONS **2,225** CITATIONS

SEE PROFILE



Contents lists available at SciVerse ScienceDirect

Tectonophysics

journal homepage: www.elsevier.com/locate/tecto

Review Article

Unraveling the geometry of the Farallon plate: Synthesis of three-dimensional imaging results from USArray

Gary L. Pavlis^{a,*}, Karin Sigloch^b, Scott Burdick^c, Matthew J. Fouch^d, Frank L. Vernon^e^a Department of Geological Sciences, 1001 East 10th Street, Indiana University, Bloomington, IN 47405, United States^b Department of Earth and Environmental Sciences, Ludwig-Maximilians-Universität, Theresienstrasse 41, D-80333, Munich, Germany^c Department of Earth, Atmospheric, and Planetary Sciences, Massachusetts Institute of Technology, Cambridge, MA, United States^d Department of Terrestrial Magnetism, Carnegie Institution of Washington, 5241 Broad Branch Road, NW, Washington, DC 20015, United States^e Institute of Geophysics and Planetary Physics (IGPP), University of California, San Diego, La Jolla, CA, United States

ARTICLE INFO

Article history:

Received 17 July 2011

Received in revised form 3 February 2012

Accepted 6 February 2012

Available online xxx

Keywords:

Farallon plate

Tomography

Seismic imaging

Mantle structure

ABSTRACT

We compare 12 recent three-dimensional (3D) seismic imaging results that made extensive use of data from the Earthscope Transportable Array (TA). Our goal is to sort out what can be said about the geometry of the Farallon plate. Our main approach is 3D visualization using a kinematic plate motion model as a framework. Comparison of results from all 12 image volumes indicates that the results are most consistent with a single, coherent Farallon slab overridden by North American. The Farallon can be tracked from the trench in the Pacific Northwest to its remnants in the lower mantle under eastern North America. From the trench the lithosphere has a low dip to the volcanic arc. Immediately east of the arc the slab steepens sharply before undergoing a decrease in dip above the 410 km discontinuity. The gently dipping section varies along strike. Under Washington the deflection is minor but to the south the slab flattens to become nearly horizontal beneath southern Idaho. There is a strong agreement that the high velocity anomaly associated with the slab vanishes under eastern Oregon. Scattered wave imaging results, however, suggest the top of the anomaly is continuous. These can be reconciled if one assumes the wavespeed anomaly has been neutralized by processes linked to the Yellowstone system. We find that all results are consistent with a 4D kinematic model of the Mendocino slab window under Nevada and Utah. In the eastern US the larger scale models all show a lower mantle anomaly related to the older history of Farallon subduction. The link between the lower mantle and new results in the U.S. Cordillera lies under the High Plains where the required USArray coverage is not yet complete. Image volumes in a unified format are supplied in an electronic supplement.

© 2012 Elsevier B.V. All rights reserved.

Contents

1.	Introduction	0
2.	Imaging volumes	0
2.1.	Overview	0
2.2.	MIT11	0
2.3.	SIG11 and TIA10	0
2.4.	DNA09 P, DNA09 S, and DNA10	0
2.5.	UO10P and UO10S	0
2.6.	NWUS11-P and NWUS11-S	0
2.7.	NA07	0
2.8.	PWMIG11	0
3.	Plate tectonic framework	0
4.	Imaged geometry of the subducted Farallon plate	0
4.1.	Overview	0
4.2.	Common geometric features	0
4.2.1.	Gorda slab downdip geometry	0

* Corresponding author. Tel.: +1 18128555141; fax: +1 18128557899.

E-mail addresses: pavlis@indiana.edu (G.L. Pavlis), sigloch@geophysik.uni-muenchen.de (K. Sigloch), sburdick@mit.edu (S. Burdick), fouch@dtm.ciw.edu (M.J. Fouch), flvernon@ucsd.edu (F.L. Vernon).

4.2.2.	Vanishing slab in the high lava plains region	0
4.2.3.	Slab geometry under Washington State	0
4.2.4.	Slab window east of the San Andreas	0
4.3.	Tests of regional scale results	0
4.3.1.	Great Basin drip model	0
4.3.2.	Idaho/Oregon high velocity anomaly	0
4.4.	Larger scale subduction geometry	0
4.4.1.	Overview	0
4.4.2.	The old Farallon slab in the lower mantle	0
4.4.3.	The big break and the Farallon slab beneath the High Plains	0
5.	Discussion and conclusions	0
6.	Electronic supplement	0
6.1.	Animations	0
6.2.	Visualization files	0
	Acknowledgments	0
	References	0

1. Introduction

The subduction of the Farallon/Kula plate system beneath the western margin of North America has been the most important mantle process shaping the continent over the past 200 Myr. During that time North America has overridden a block of oceanic lithosphere as large as the present-day Pacific basin (e.g., [Dobrovine and Tarduno, 2008](#); [Engebretson et al., 1985](#)). This ancient seafloor was produced by an enormous spreading ridge system) that grew the Farallon/Kula plates to its east, and the Pacific plate to its west (e.g., [Atwater, 1989](#)). Today the Farallon plate has subducted almost completely under the western margins of the Americas. Its last remnants are the Juan de Fuca, Gorda and Explorer microplates located offshore in western North America, and the Nazca and Cocos plates that abut Central and South America.

The geological literature about this plate system is vast; even a cursory electronic literature search for the keywords “Farallon and Kula” results in thousands of citations. The evolution of the Farallon/Kula plates is mostly constrained by magnetic anomalies on the Pacific seafloor, which is the surviving conjugate plate ([Engebretson et al., 1985](#)). Direct seismological imaging of the subducted plate was data-limited before the advent of the USArray experiment. The global body-wave tomographies of [Grand \(1994\)](#) and [van der Hilst et al. \(1997\)](#) picked up on the Farallon’s massive deep end in lower mantle beneath eastern North America and the Atlantic. The surface-wave inversion of [van der Lee and Nolet \(1997\)](#) found the plate fragmented close to the trench, in the uppermost mantle of western North America. The images of these shallow western fragments were refined somewhat in the decade that followed (e.g. [Nettles and Dziewonski, 2008](#)), but their connection to the eastern lower-mantle slab remained in the dark, since central North America was only sparsely instrumented. Hence one of the original goals of the first Earth Scope science plan was to understand the space-time evolution of the Farallon/Kula system.

This paper is focused on seismic imaging results that have been published since the start of the USArray. At the time of writing, the Transportable Array component is located approximately over the High Plains of the central U.S., but due to publication lags, the highest-resolution results so far have been obtained for the mantle under the Cordillera. Hence that area will be our prime focus, but the final sections also consider current models of the larger-scale Farallon geometry under the entire continent.

We examine 12 recent mantle models: 9 body-wave tomography models, one pure surface-wave tomography model, one hybrid surface and body-wave model, and one 3D wavefield image volume. We do not attempt a traditional literature review, i.e. a synopsis of papers published about the models. Rather, we wanted to explore the volumetric data sets themselves, using state-of-the-art, 3-D

visualization techniques. This gives a more immediate grasp of the complex subduction geometries and provides a means of comparison impossible with the printed medium. An important goal was to enable every reader to do the same, by providing all 12 volumetric data sets as an electronic supplement. The original models were provided by their authors in different electronic formats, some of them not published with the original papers. Here we make them available as resampled, unified model volumes in a standard file format (Visualization Tool Kit ([Schroeder et al., 2006](#)) files directly loadable by the powerful, open-source visualization software Paraview).

While investigating a wide sampling of recently published models, our effort cannot be exhaustive. Our primary focus is limited to understanding the 3-D geometry of the subducted Farallon plate. This led us to focus on recent, regional, body-wave models. These P- and S-wave models afford the highest resolution possible today over the entire possible depth range under the dense USArray. The wavefield imaging volume offers a complementary view in the body-wave domain, by highlighting material interfaces ([Pavlis, 2011b](#)). We also include one surface-wave tomography for comparison ([Bedle and van der Lee, 2009](#)), but these data – whether in their traditional form or using noise cross-correlation imaging – are less suited to our purpose because they illuminate shallower structures. Including the Bedle and van der Lee model helps to clarify that point.

We assert that this paper is important for three reasons. First, it provides the first comprehensive comparison of the collection of imaging results obtained from USArray data to date. It provides a comprehensive model for the geometry of the Farallon slab in the mantle that can and should be used as a starting point for future studies. Second, although we focus on the Farallon geometry problem we stress that the supplement contains electronic files that will allow anyone in the community to do similar comparisons to address other problems. We hope this will provide a means for other people in the community to make more effective use of results from the USArray. A wide range of other scientific questions other than the Farallon slab geometry could be addressed more objectively by comparison of this suite of results in the true geometric relationship. Finally, this paper contains an important new, original result on the nature of the Mendocino slab window. We confirm the kinematic model of the classic papers by [Dickenson and Snyder \(1979a,b\)](#) and extend that model in the third dimension.

2. Imaging volumes

2.1. Overview

We examined twelve seismic imaging results with properties summarized in [Table 1](#). This section expands on each row of [Table 1](#). The main purpose of this section is to provide a clear link to

Table 1

Summary of sources and properties of seismic imaging results reviewed in this paper.

Acronym	Properties	Data type	Number data	Crustal Correction	Method	Scale
MIT11	V_p	P time picks made by USArray ANF	1.9×10^7 global P picks 1.6×10^6 USArray picks	CRUST 2.0	Ray tomography method of Li et al. (2008)	Global
SIG11	V_p	Cross correlation time and amplitude in multiple bands	369,829 P times, 59,801 amplitudes	CRUST 2.0 (Basin et al., 2000)	Multi-band finite frequency tomography	Global
TIA10	V_s	Cross correlation time and amplitude in multiple bands	98,371 SH times, 74,655 S amplitudes, 8270 SS-S differential times, 1788 Love wave phase delays	CRUST 2.0	Joint inversion of finite frequency body wave times and amplitudes with Love wave phase delays	Global
DNA09P DNA09S	V_p and V_s	Relative P and S times in multiple frequency bands	58,690 P phases 34,850 S phases 3900 SKS phases	Modified CRUST2.0	Finite frequency tomography. Joint P and S inversion	Regional
UOP UOS	V_p and V_s	Relative P and S times in multiple frequency bands	248,000 P phases 84,000 S phases	Modified CRUST2.0	Finite frequency tomography. Joint P and S inversion	Regional
CIASP CIASS	V_p and V_s	P and S times measured by multichannel cross correlation	79,212 P phases 88,689 S phases	Station correction	Ray tomography method of VanDecar (1991)	Regional
NA07	V_s	Vertical component waveforms windowed on Rayleigh wave	5549 waveforms	Van der Lee and Frederiksen (2005) plus EARS	Partitioned waveform inversion method of van der Lee and Nolet (1997)	Global
PWMIG11	S-P scattering potential	EARS P receiver functions	138,666 seismograms (5×10^8 data points)	NA	Plane wave migration inversion method of Poppeliers and Pavlis (2003a,b)	Regional

original sources. We also aim to summarize variations in resolving capability of the different methods and data sets used in the different results.

2.2. MIT11

The MIT model, MITP_USA_2011MAR, was obtained via a linearized global inversion of *P*-wave traveltime residuals. The details of the methodology used are described in depth in Li et al. (2008) and Burdick et al. (2008). The minimum grid spacing for the inversion is $0.3^\circ \times 0.3^\circ \times 45$ km beneath areas of North America with sufficient data density, but the spacing is adapted based on raypath coverage in each mantle volume. The inversion is linearized about the 1D reference Earth model, ak135 (Kennett et al., 1995). Teleseismic raypaths are calculated through ak135 and wavespeeds in the mantle are perturbed around it. In order to prevent strong heterogeneity from the crust from creating artifacts in the mantle, a crustal correction is also applied. The global reference crustal model CRUST 2.0 is projected onto the inversion grid and values of the crustal part of model are held close to it.

The inversion was performed using ~1,650,000 USArray traveltime residuals from between 2004 and March 2011, picked by the Array Network facility (<http://anf.ucsd.edu>). The data used also included ~10 million global *P*-wave traveltime residuals from the bulletin of the International Seismological Centre which have been reprocessed using the methods described by Engdahl et al. (1998). This model is an update from Burdick et al. (2010) so we call it MIT11.

2.3. SIG11 and TIA10

The *P*-wave model SIG11 and the *S*-wave model TIA10 were obtained using a multiple-frequency tomography technique. This waveform-based method interprets traveltime and amplitude anomalies derived from the cross-correlation of observed seismograms with their forward-modeled counterparts. Multi-frequency tomography can be regarded as “second generation” finite-frequency tomography. Both methods explicitly model the scattering of seismic wave energy by the imaging targets (i.e., mantle heterogeneities). So-called sensitivity kernels map out the spatially extended Fresnel zones that influence the measurements and thus constrain the inversion; sensitivity kernels of teleseismic *P*- and *S*-waves are banana-shaped (Dahlen et al., 2000; Tian et al., 2007).

The first finite-frequency inversions (e.g., Montelli et al., 2004) re-interpreted existing, mostly hand-picked, traveltime data relaxing the high frequency approximation of ray theory made in all older tomography methods. Since then, new data analysis methods have been developed that provide data sets that exploit the full potential of finite-frequency theory that were applied to produce this solution (Sigloch and Nolet, 2006). This yields 5 to 10 time lag and amplitude measurements for each seismogram instead of the single time lag measurement made by conventional “picking”. Each datum is linked to a different sensitivity kernel, which expands the amount of information extracted from each seismogram.

North America was the first large-scale testbed for this method (Sigloch, 2011; Sigloch et al., 2008; Tian et al., 2009, 2011). The SIG11 *P*-velocity model includes all teleseismic waveforms of sufficient quality recorded between Jan. 1, 1999, and July, of 2007 at the U.S., Canadian, and Mexican broadband stations available through the IRIS DMC. The majority of these measurements were made from USArray data, but temporary and permanent stations in the Central and Eastern U.S. provide important additional data. 635 earthquakes ($m_b > 5.8$) and 1118 receivers yielded 59,801 good broadband wave paths. Traveltime measurements were made in seven overlapping frequency bands (center periods between 21 s and 2.7 s); amplitudes were measured in three bands centered on 21 s, 15 s, and 11 s. A total of 369,827 traveltime data and 160,027 amplitude data passed the quality control.

The TIA10 *S*-wave model is a joint inversion of SH traveltime delays, SS differential traveltime delays, and Love wave phase delays. It uses data assembled from the IRIS archives through October of 2008. For the body waves, five passbands centered on periods of 40, 20, 10, 5 and 2.5 s were used. 26,296 unique SH paths yielded 98,371 traveltimes, and 74,665 amplitudes in the three low bands (Tian et al., 2009). 8270 SS-S paths yielded 18,919 differential delay data in the three low bands. The surface wave data came from the global data set of Zhou et al. (2006): 1778 minor-arc Love wave paths resulted in 19,485 fundamental mode phase delays measured at 11 frequencies (5, 6, ..., 15 mHz).

The SIG11, TIA10, and MIT11 models should be viewed as complementary results that are more internally compatible with each other than any of the other tomography models. All used a mix of global and regional scale data. The data and the details of the techniques are very different, but they are important in providing a broader context compared to any of the other image volumes. The most basic reason is coverage. All the other results are limited to the western U.S.

while these three models can be thought of as high resolution models of the western U.S. embedded in a 3D global reference model.

2.4. DNA09 P, DNA09 S, and DNA10

We used three tomography models available electronically from the Dynamic North America web site at the University of California, Berkeley (<http://seismo.berkeley.edu/~rallen/research/dna/>). DNA09 P and DNA09 S are models used by Obrebski et al. (2010) and DNA10 is the model used by Obrebski et al. (2011). The DNA09 models were produced from teleseismic P and S phase delays measured using waveform cross-correlation in multiple frequency bands. Because they use frequency dependent arrival residuals they use a form of multi-frequency tomographic inversion with the benefits discussed in Section 2.3. The paper by Obrebski et al., (2010) provides minimal information on the code they used for this solution or its theoretical foundations, but Obrebski et al. (2011) references the now classic reference on finite frequency tomography by Dahlen et al. (2000). Both methods are properly viewed as being siblings of the SIG11 and TIA11 with a more regional-scale focus. A key point is that the DNA09 P and S models were estimated from body wave travel time residuals alone and they were estimated in a joint inversion. That is, both the P and S models are estimated together. DNA10 used a novel joint body wave and surface wave inversion method that merges the body wave method used in Obrebski et al. (2010) with the surface wave method of Pollitz and Snoke (2010). The body wave data used in Obrebski et al. (2011) appears to be a more conservatively edited subset of the data used by Obrebski et al. (2010). The DNA09 models used a standard crustal correction, but the details are not completely clear from their paper. The DNA10 model aims to use surface waves to improve crustal structure, and the implication in the paper is that crustal models are used only to produce a better starting model for the inversion.

2.5. UO10P and UO10S

We used the P and S tomography models applied in publications by Schmandt and Humphreys (2010a, 2011). Schmandt and Humphreys (2010a) give a brief summary of the data and method used to produce these results. The method used by Schmandt and Humphreys is similar to Obrebski et al. (2010), although the degree of common ancestry is unclear. As with the DNA models they measured delay times from teleseismic P and S phase using waveform cross-correlation in multiple frequency bands. Thus the data being used and the inversion method are genetically similar to that of the DNA09 models described in Section 2.4. A related paper by Schmandt and Humphreys (2010b) provides a more complete description of the method. In many respects this pair of models and the DNA09 models (Section 2.4) should be most comparable. Both results use the same data kernels, both are joint P and S inversions, both use only teleseismic P and S phases measured in multiple bands, and both apply a similar set of crustal corrections. There are two primary distinctions between the UO10 and DNA09 models. First, the data are different. The data set used by Schmandt and Humphreys is considerably larger and included data from the High Lava Plains Experiment not utilized by Obrebski et al. (2010) while the DNA models used additional stations in two different temporary experiments (FACES and FAME) not available to Schmandt and Humphreys. The measurements were also made independently. The second difference between these two results is that both models have a number of independently adjusted, tunable inversion parameters that are not all spelled out exactly in the existing publications. The combination of these two differences is undoubtedly the reason for differences in the results.

2.6. NWUS11-P and NWUS11-S

One of the earliest body wave tomography models computed from USArray data was that of Roth et al. (2008). Here we use an updated version of that model from James et al. (2011) (models NWUS11-P and NWUS11-S; P and S refer to P and S velocities). The original tabulation of these models can be found at http://www.dtm.ciw.edu/research/HLP/tomographic_models, while the version readable by paraview is in the supplement of this paper.

Data for NWUS11-P and NWUS11-S are P and S relative delay times estimated using the multichannel cross-correlation method of VanDecar and Crosson (1990). These models differ from the multifrequency methods used in DNA09P, DNA09S, DNA10, UO10P, and UO10S because this measurement method utilizes only a single frequency band and therefore yields only one datum per seismogram. The inversion does not include frequency-dependent kernel information, but rather the “infinite frequency” (ray-based) method of VanDecar (1991). These models do not use a crustal correction and depend only on static station corrections to account for crustal anomalies. They also include hypocenter locations as free parameters. Finally, unlike the DNA09 and UO10 models the P and S solutions are computed independently instead of as a simultaneous method. This is justified because the baseline for each model is different based on the relative delay time measurements.

2.7. NA07

Bedle and van der Lee (2009) recently applied the partitioned waveform inversion method of van der Lee and Nolet (1997) to a suite of 5549 waveforms recorded on stations throughout North America including early data from the USArray. This S-wave model was produced by waveform inversion of fundamental and higher mode Rayleigh waves alone. It thus has drastically different resolution properties than any of the other models in this suite that all used body waves. Like the DNA10 model the resolution gets progressively poorer with depth because of its dependence on surface wave data. This is an even larger issue for NA07 than for DNA10 because this solution is a pure surface wave model. In the context of this paper NA07 is best viewed as a high resolution, global surface wave model. High global scale resolution, however, is a very low resolution relative to the any of the body wave models to which we are comparing NA07. We include NA07 largely for completeness because it is an openly available model derived from USArray data. The lower resolution of this model in the transition zone and lower mantle made this model of little use for this study, but others work focused on shallower parts of the earth might find it useful. NA07 also illustrates graphically why we elected to not include other velocity models produced only from surface wave data.

2.8. PWMIG11

The last three-dimensional image volume we have used in this study is an update of the results discussed by Pavlis (2011b). This result is based on the plane wave migration method described by Poppeliers and Pavlis (2003a, 2003b) implemented in a fully three-dimensional form with the algorithms described by Pavlis (2011a). The method provides a fully 3D image of the subsurface at the scale of the entire continent. It adds constraints that are complementary to the information provided by any of the tomography models. There are several fundamental differences between this image and any of the tomography models:

1. The tomography models represent variations in P or S wavespeed relative to some radially symmetric earth model while the wavefield image is an estimate of P to S conversion scattering strength at every point in the medium. The relationship between the two

is best understood by a close analog to the seismic reflection method: the wavefield image is comparable to a 3D seismic reflection image volume while the tomography models are comparable to a velocity model used to migrate the data. Therefore we refer to the wavefield results as an “image volume” instead of a “model”.

2. A corollary of item 1 is that the wavefield image volume defines discontinuities in physical properties of the medium while tomography models are all smoothed representations of the real seismic velocity field. For instance, later we show a correlation of a continuous, dipping conversion horizon in this image volume with a strong gradient in velocity seen consistently in tomography models. The implication is that this particular gradient in physical properties is sharp enough to generate significant P to S scattering. Tomography models smear out such discontinuities as an inevitable cost of regularization, which is essential to stabilize the inversion. The methods are complementary. Tomography models resolve smoothly varying structure that scattered wave images cannot detect. Conversely, all the tomography methods cannot detect the shorter wavelength structure that generates P to S conversions.
3. The data used to construct the image volume are completely different. The tomography models are constructed mainly from travel time residual data, which in some cases use a frequency dependent model of scattering (Section 2.3). We note that SIG11 also includes amplitude variations, which provide additional constraints on the velocity perturbations in the final tomography model. The common theme is that all tomography methods use parametric data derived from raw waveforms. Wavefield imaging, in contrast, is a direct imaging method closely related to the seismic reflection method. The plane wave method used here utilizes so-called receiver function estimates produced by the EARS (Crotwell, 2007; Crotwell and Owens, 2005) project as data. Receiver functions are an approximation of the impulse response of the subsurface to an incident, teleseismic P wave, produced by deconvolution of an estimate of the source wavelet. The input data to the plane wave migration code of Pavlis (2011a) are seismograms that are assumed to be estimates of the P to S scattering response of the medium.
4. The image reconstruction approach is fundamentally different. All tomography models use some form of large-scale matrix inversion to estimate wavespeed variations within the medium that fit the parametric data derived from the original waveforms. All use some form of regularization to stabilize the inversion. Although essential to produce anything meaningful, regularization comes at the inevitable cost of rendering the model smooth in some sense. The plane wave method used here (Poppeliers and Pavlis, 2003a), however, is based on an analytic inverse called the inverse generalized Radon transform (IGRT). The fancy name clouds the much simpler concept behind this method (Pavlis, 2005), which is to provide a mathematically correct way of implementing a simple imaging model, and to reconstruct the image as a linear combination of all the data points that satisfy the propagation model for single-scattering P to S conversions. The IGRT simply provides the recipe to define the weights in the linear combination (Pavlis, 2005).

PWMIG11 is an update of an earlier result described by Pavlis (2011b); the same algorithms and set of control parameters were used to compute the updated imaging volume. The difference is that the present result was produced from a data set that was improved in two ways. First, the number of seismograms is larger and the area of coverage is significantly better than in Pavlis (2011b). This result uses approximately 18 months of additional TA data. In addition, data from the SNEP experiment were released to the broader community and are part of this new image. This removed a major hole in the earlier data for southern California. Secondly, the data in this study

and the Pavlis (2011b) paper were auto-edited by a set of rules defined by the automated system called EARS (Crotwell and Owens, 2005). Pavlis (2011b) used an early, prerelease version of the EARS data set that had a number of issues that seem to have been largely resolved in the newer data. Most importantly, the results in southern California in the Pavlis (2011b) paper were largely wiped out by what appear to have been a handful of bad seismograms estimated from stations in the Los Angeles region. The problem seems to have disappeared in results presented here. This is almost certainly due to improvements in quality control on the final released version of the EARS data product.

3. Plate tectonic framework

Fig. 1 provides a framework for this paper in two ways. First, it serves as a base map for the paper along with a companion Fig. 2. Second, it provides what we will call a tectonic framework based on the simplest model one can cast for the geometry of the Farallon slab (Fig. 3). We will refer to this model as the “single slab model surface” (Figs. 4–8). The geometry is a continuous, warped surface seen in a 3D representation in Fig. 3 and in a more conventional map view in Fig. 1.

We note that this surface is based on a model of the system that may have little relationship to reality, but it nonetheless provides a useful, three-dimensional reference frame (Fig. 3) that provides kinematic 4D (Fig. 1) constraints on the Farallon system. The concept is to define a natural set of generalized coordinates for a surface linked to plate motion in three dimensions. The coordinates used here are similar to those defined by Pavlis (2011b). We used the same set of control points described in that paper to define this surface. These come from three sources: (1) the existing trench defines the surface where subduction is still active; (2) control points are placed at 125 km below active volcanoes; and (3) points are picked from joint interpretation of tomography models and the earlier version of the converted wave image used by Pavlis (2011b). These control points were supplemented by three simplified control points from Grand (1994) to provide a crude extrapolation of the surface to the deeper mantle. Specifically the surface was constrained to intersect a depth of 1375 km at the following three points: 65° W, 70° N; 75° W, 42.5° N; and 80° W, 20° N. The working surface was then interpolated by Delaunay triangularization and meshed with what 3D visualization systems commonly call a structured grid (e.g. Schoeder et al., 2006, Chap. 8). Here the structured grid is a surface defined by a mesh of points that are topologically equivalent to a rectangle. The origin of the coordinate system is at the current triple junction location at Cape Mendocino, California. Lines of constant x_2 define a suite of curves that can be viewed as flow lines for a particular plate motion model. The model shown in Figs. 1–3 uses the recent plate motion model for Farallon–North America computed by Doubrovine and Tarduno (2008) to define these curves. This differs from Pavlis (2011b) who used a single plate pole based on an estimate of current plate motion.

To clarify the geometry notice that the $x_2 = 0$ curve, which is topologically equivalent to the x -axis of the standard Cartesian x – y axis graphic representation, is shown in Fig. 1 as beginning at Cape Mendocino and running to the Canadian border in the northwest corner of North Dakota. The complementary coordinates are lines of constant x_1 , which are an approximation of time since subduction. The approximation is that the surface follows a rigid plate that does not undergo any shortening or extension. This is a simplistic description of reality, since below the base of the lithosphere the slab almost certainly is undergoing some level of compression or extension, but this geometry provides a useful set of generalized coordinates nonetheless. This model also neglects distortion created by growth (erosion) of the trench that would tend to push the time zero curve further west (east) with time. In any case, the $x_1 = 0$ curve in Fig. 1

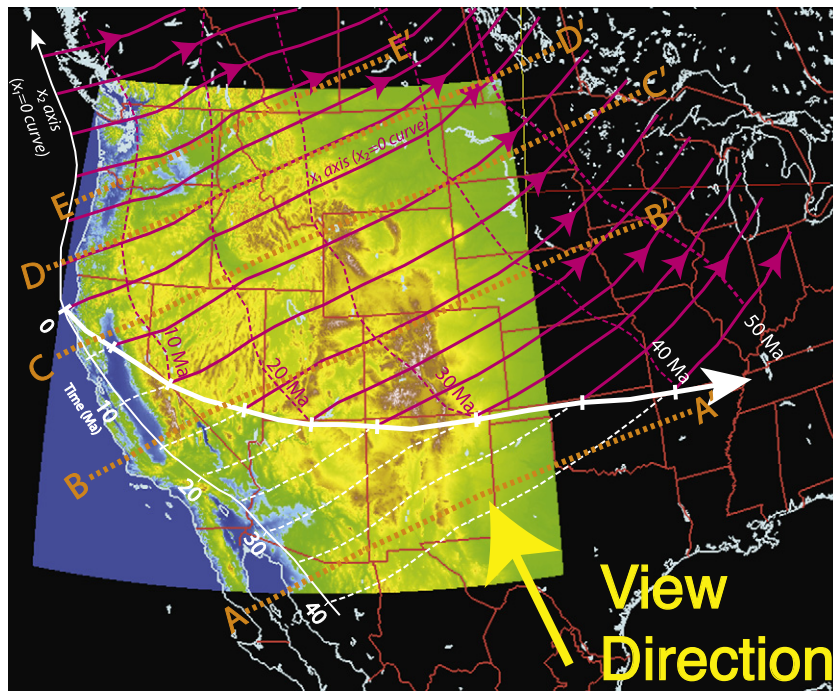


Fig. 1. Basemap for western US region. Cross-section trajectories are illustrated with dashed, orange lines with labels of AA', BB', etc. related to Figs. 4–8. The figure is a 3D projection looking radially downward from a point near the center of the scene and not a normal map projection. The map base shows topography colored by elevation with coastline data (light blue lines) and state and national boundaries (red lines) overlain. The magenta lines are the projection of flow lines on the top of the single surface slab model described in the text. The dashed white lines are backward projected flow lines related to this surface. The heavy white line shows an approximation of the upper limit of the Farallon slab (upper limit of slab window) using this 3D model of the surface. The time shown is time since termination of subduction by passage of the Mendocino triple junction.

(y-axis equivalent) for positive x_2 is the current location of the trench. The time lines illustrated in Figs. 1 and 2 are downdip projections of the $x_1 = 0$ curve based on the simple rigid plate approximation with a time-invariant trench.

Defining the trajectory for the $x_1 = 0$ curve (y-axis equivalent) south of Cape Mendocino ($x_2 < 0$) is more problematic since there is

not an unambiguous curve for zero time. The reason is related to the widely accepted “Slab Window” model first suggested by Atwater (1970) and with kinematics described in the now classic papers by Dickinson and Snyder (1979a,b). South of the Mendocino transform fault, the Farallon–Pacific ridge was offset towards the east and has been gradually overridden by North America since

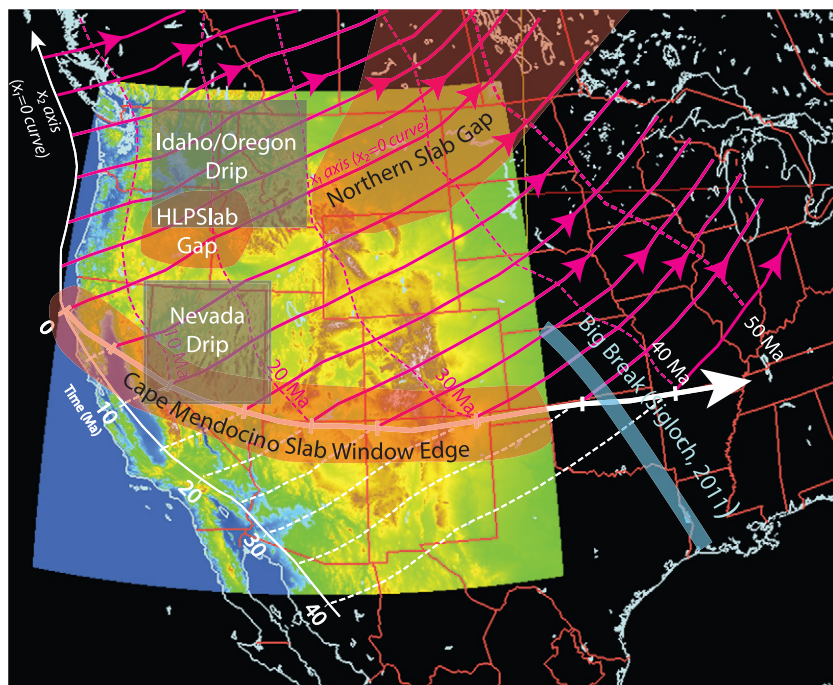


Fig. 2. Geographic location of features discussed in this paper. The basemap for this figure is the same as Fig. 1. The map illustrates the approximate geographic extent of features discussed in the text with translucent overlays.

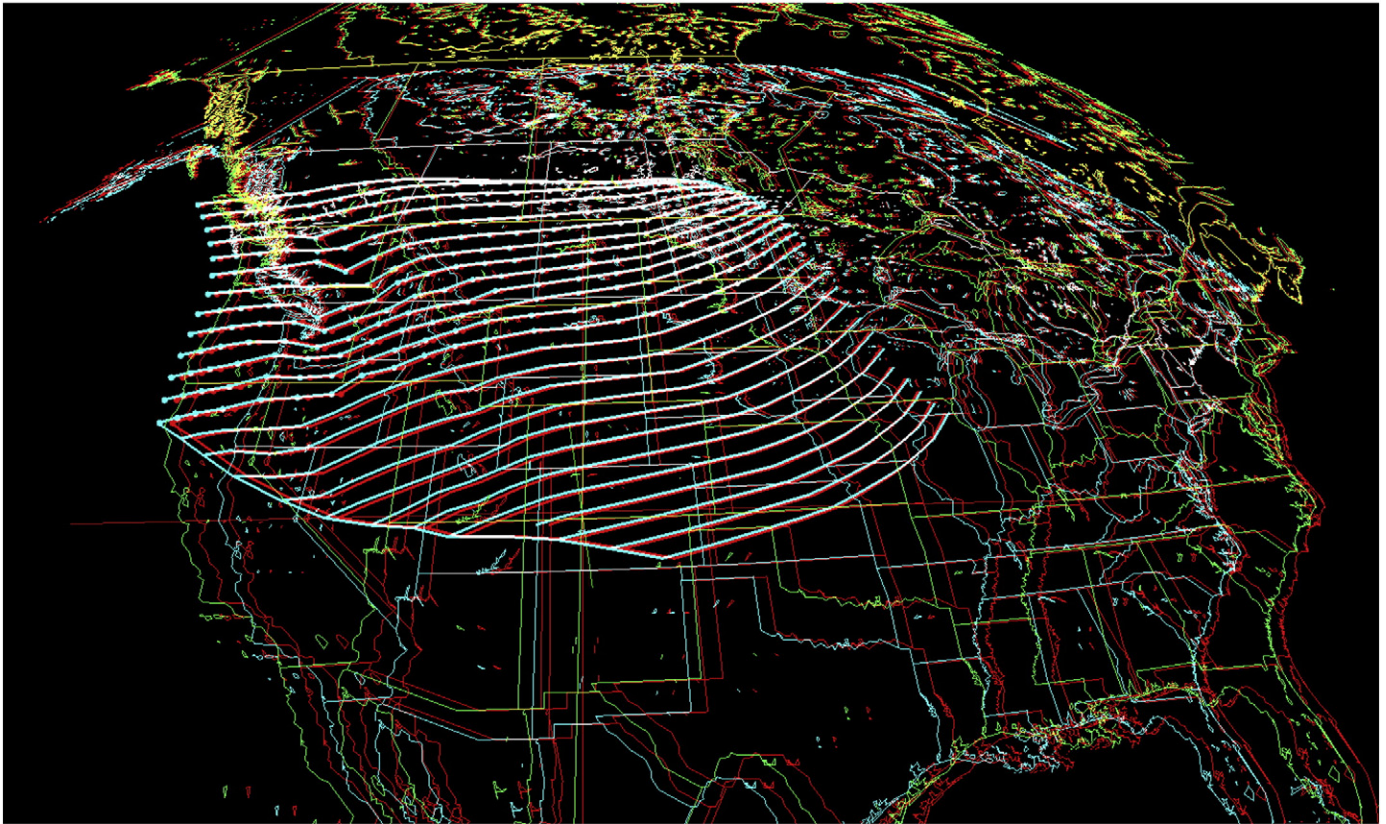


Fig. 3. Three-dimensional representation of single surface slab model. Figure is an anaglyph stereo pair than requires a pair of colored stereo pair glasses to be seen in stereo. This figure and similar stereo pairs later in this paper are best viewed electronically as not all hardcopy ink will provide the right color mix to properly separate the two images. The flow lines computed for this three-dimensional model are shown in white. For flow lines north of Cape Mendocino tic marks are placed along the curves at 2.5 Myr intervals. Geographic line data provides a reference position for this three-dimensional surface geometry. The yellow curves are at the surface of the earth. The white geographic line data are projected to a depth of 400 km to provide a depth standard.

~40 Ma. Thus the San Andreas transform developed through northward propagation of the Mendocino triple junction. We modeled this process quantitatively by defining the $x_1 = 0$ curve south of the triple junction as the trace of the current triple junction backward in time relative to fixed North America. For consistency we used stage poles for Pacific–North America from the same model by [Dobrovine and Tarduno \(2008\)](#) used to define the Farallon–North America flow lines. This model provides a useful three-dimensional prediction of the western limit of the Farallon slab illustrated in [Fig. 1](#). We emphasize that this is based on two approximations: (1) the same rigid plate approximation noted above, and (2) it ignores the known geometry from of the trailing edge of this system that could potentially be derived from sea floor spreading anomalies in the Pacific (e.g. [Atwater, 1989](#)). When viewing the tomography models relative to this surface the reader should take the pragmatic view that the edge shown in [Fig. 1 and 3](#) can be easily moved around in any direction by at least 100 km.

4. Imaged geometry of the subducted Farallon plate

4.1. Overview

Our focus is 12 individual three-dimensional volumes each defining one of three different physical properties: P-wave velocity, S-wave velocity, and P to S scattering potential. The amount of information contained in all of these results is enormous. To keep the discussion tractable we focus on evaluation of features of the geometry of the Farallon slab that have been suggested in publications to date. We emphasize that the best way to evaluate the ideas presented in this paper is to view the results independently using 3D visualization

with the full suite of files supplied in the electronic supplement. Static figures can be made prettier, but can only go so far in presenting an unambiguously three-dimensional problem like this one.

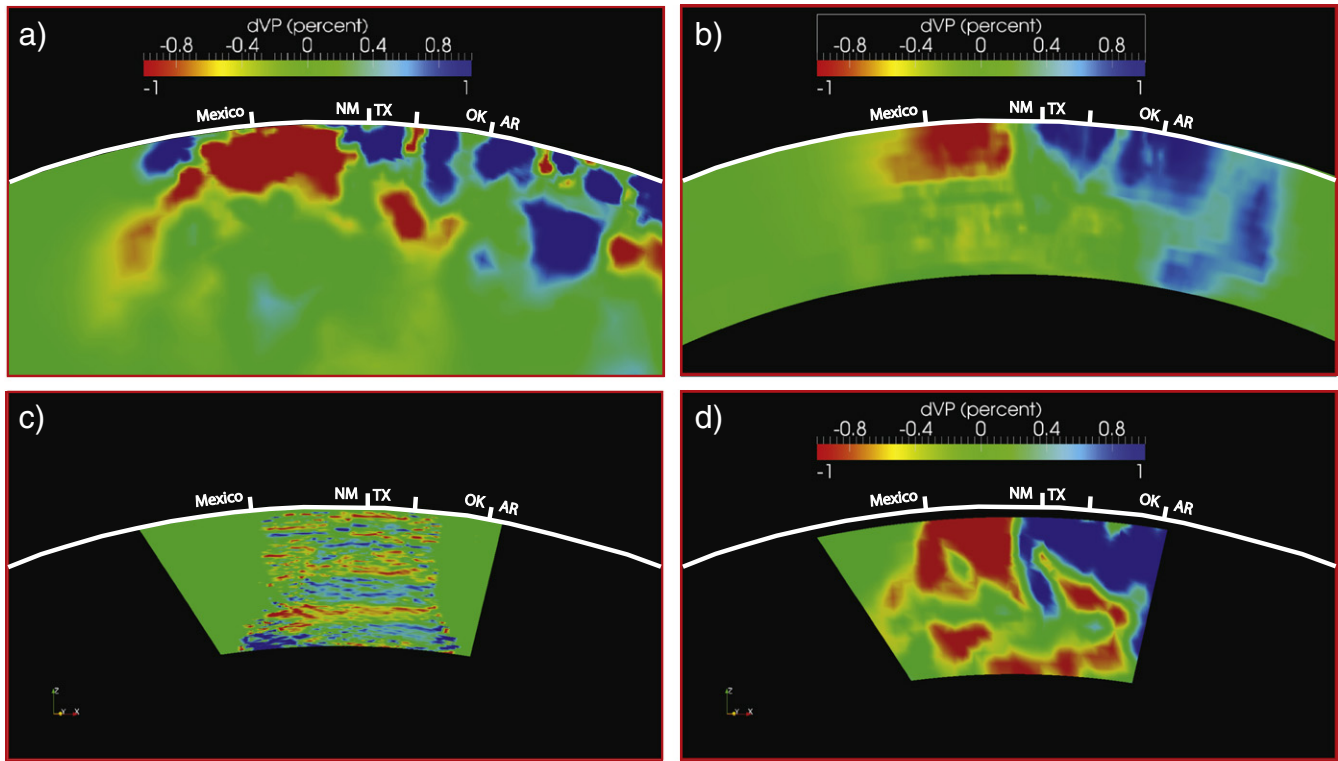
We note a final, general issue: it is a major challenge to evaluate results like these objectively. The fundamental reason is that seismic tomography results today are commonly presented as a result without any standardized error metrics. It is thus extremely difficult to evaluate if a particular blue or red blob in isolation is meaningful. As a result the approach used here is graphical. We simply look for common features in the different results and judge them against interpretations presented to date in the literature.

4.2. Common geometric features

4.2.1. Gorda slab downdip geometry

The clearest component of the Farallon slab imaged to date is seen in section CC' ([Fig. 6](#)). All of the tomography models in this section show a steeply dipping, high velocity body in the vicinity of the volcanic arc in northern California. Within the area of this section most of the results ([Fig. 6](#)) are consistent with the “single slab model surface” shown as marking the top of this feature. The tomography models show this as a fast wavespeed region below the single slab model surface or at least an area of neutral velocity variation sandwiched between lower relative velocities. The converted wave image ([Fig. 6e](#)) shows a dipping feature that was used to define the single slab model surface illustrated in these sections ([Pavlis, 2011b](#)). [Fig. 6e](#) also shows a parallel disruption of the 410 km discontinuity revealed by PWMIG11. The combined results indicate that in this region the Farallon slab is suspended in the vicinity of the 410 km discontinuity.

P-wave Models



S-wave Models

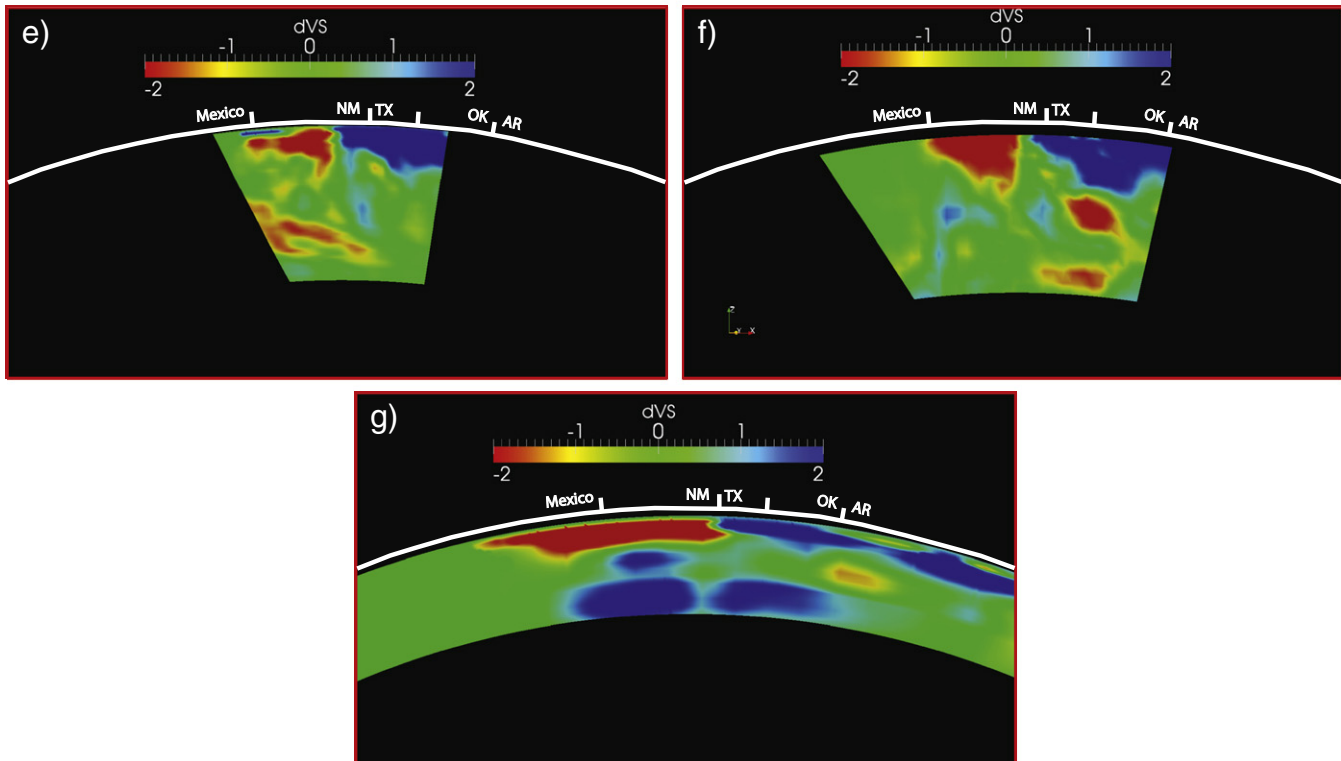
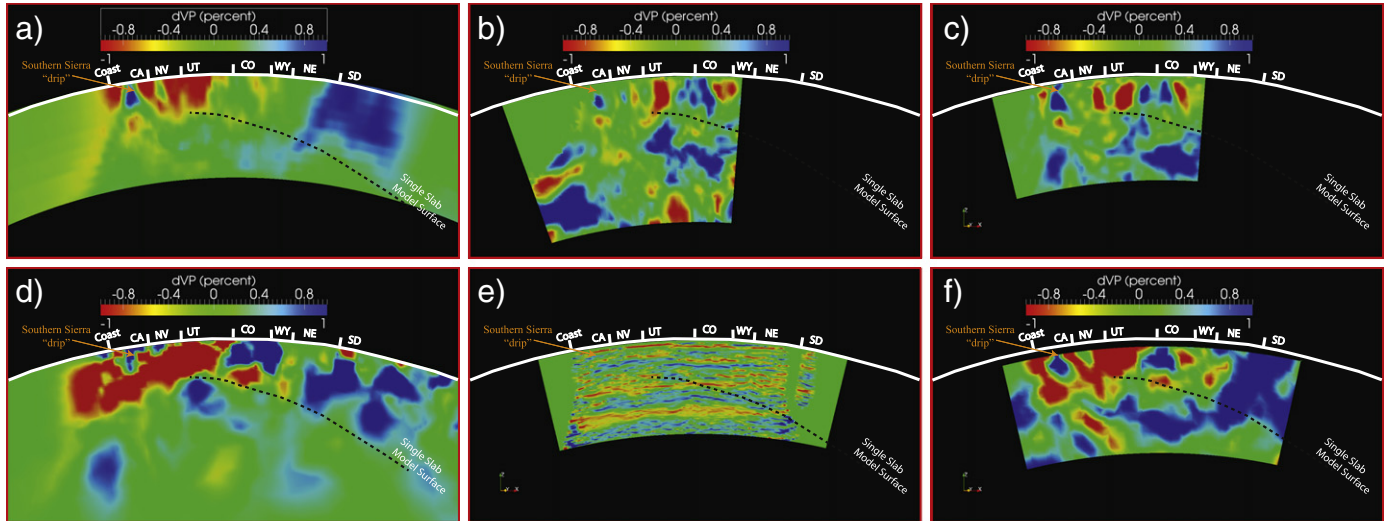


Fig. 4. Section AA' – Gulf of California to Arkansas. All sections are viewed from the southeast as illustrated in Fig. 1 and slice exactly the same section of each volume. The white line on each section is the Earth's surface with geographic boundaries marked by radial, white colored tic marks. States are defined by standard two character postal abbreviations. Tomography models all show fast velocities as blue and slow velocities as red with the scaling shown on each section. The scattered wave image result (c) shows positive P to S conversion scattering potential in red and negative conversion as blue. The color map is the same as the tomography models but reversed and scaled differently. In this and all subsequent sections of the converted wave image no scale is shown. This is done because the scattered wave image in (c) was passed through an AGC operator to provide sufficient dynamic range to compensate for the large amplitude differences between the Moho and deeper mantle conversions. (a), (b), and (d) are P wave tomography models SIG11, MIT11, and UOP (Table 1) respectively. (e)–(g) are S wave models DNA09S, UOS, and NA07 respectively.

Section BB'

P-wave Models



S-wave Models

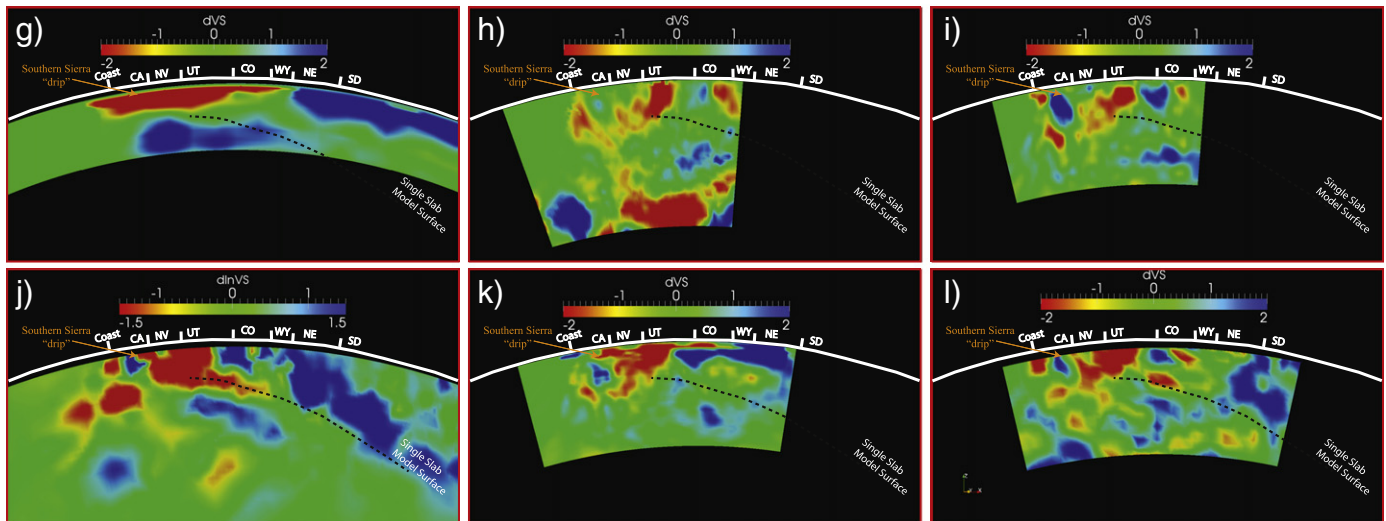


Fig. 5. Section BB' — southern California to Iowa. Color scheme and graphical components are as described in the caption to Fig. 2. P-wave tomography results are as follows (codes are defined in Table 1): (a) MIT11, (b) NWUS11-P, (c) DNA09P, (d) SIG11, (f) UOP (e) is PWMIG11. S-wave tomography results are in the lower panel have this association: (g) NA07, (h) NWUS11-S, (i) DNA09S, (j) TIA10, (k) DNA10, and (l) UO10S.

A notable exception is Obrebski et al. (2010) (sections shown in Fig. 6c and i) who suggest the steeply dipping horizon seen in their P and S models is a continuous piece of the Farallon slab. In addition, they show an east–west cross section through central Nevada and suggest the slab is fragmented in two sections. We suggest this is likely an incorrect interpretation that is not supported by the other results. It illustrates a pitfall in interpretation of a three-dimensional problem without attention to the kinematics of the deformation field. They base that interpretation on an east–west cross section which Fig. 1 shows at an azimuth rotated by almost 45° from the direction of relative plate motion. The section they use for this interpretation passes over the “Great Basin drip” (see Section 4.2.1), which we suspect has smeared across their image to lead to this conclusion. The results of this paper suggest the double slab illustrated in Obrebski et al. (2010) may be a projection artifact.

4.2.2. Vanishing slab in the high lava plains region

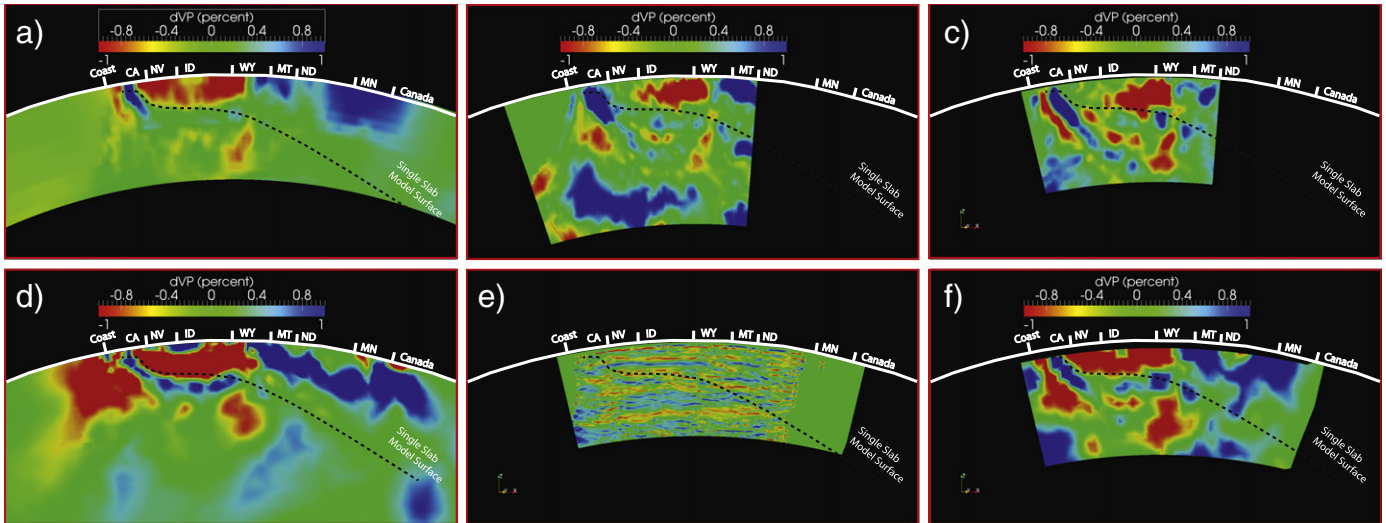
One of the earliest new observations from the USArray was the suggestion of a “slab gap” under eastern Oregon (Sigloch et al., 2008). This was further reinforced in the related study by Tian et al. (2009), who applied a similar methodology for S-wave data, by

Obrebski et al. (2010), independently by Schmandt and Humphreys (2010a,b), and most recently by James et al. (2011). This observation is well supported by all the models in section DD' (Fig. 7). All tomography models indicate that the top 200–300 km of the upper mantle in eastern Oregon is anomalously slow. Most of the tomography models indicate a shallow, fast anomaly in western Oregon where it is entirely expected: between the trench and the volcanic arc.

The geometry of the Farallon slab downdip from eastern Oregon slow anomaly is, on the other hand, more variable. All the tomography models show positive velocity anomalies at depths below around 300 km in section DD' west of the OR-ID border. The details of the geometry are, however, drastically variable and best defined as inconsistent sets of blue blobs. The converted wave image (Fig. 7e), in contrast, shows a bright, positive conversion horizon that crosscuts the negative velocity anomalies seen in the tomography models under eastern Oregon. This dipping horizon is at the same relative position as the comparable feature seen in Fig. 6e closely associated with the “simple slab model surface”. This relationship led Pavlis (2011b) to suggest that the horizon is the top of the slab, and that the surface defined by this discontinuity is continuous across the entire Cordillera of the western U.S. If this is true it implies that the process that

Section CC'

P-wave Models



S-wave Models

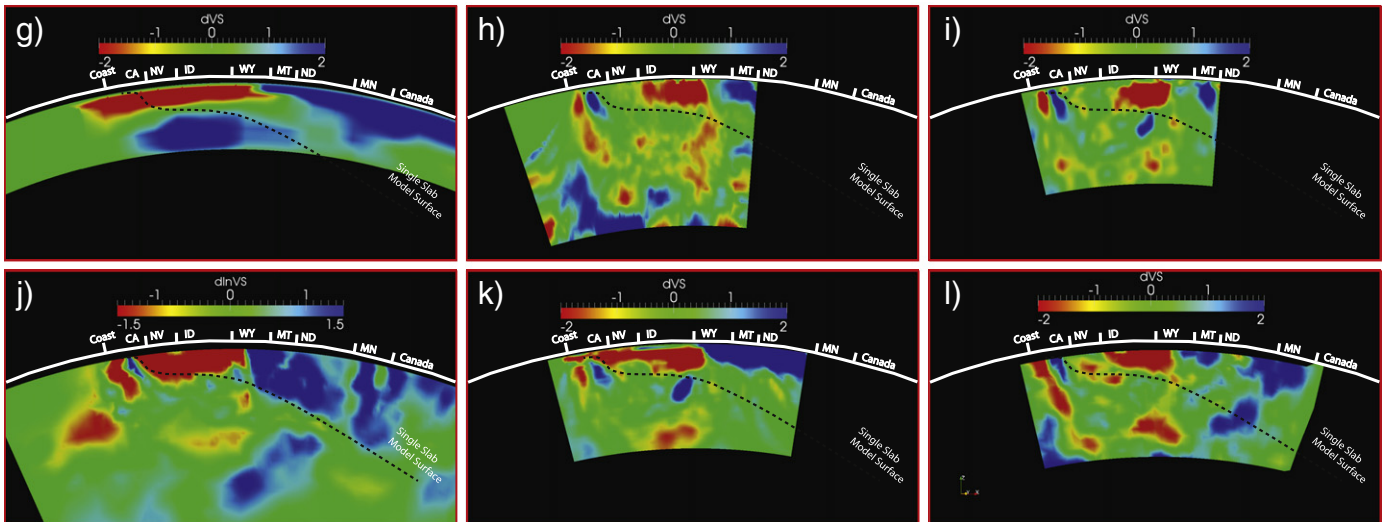


Fig. 6. Section CC' – Cape Mendocino to Canada–Minnesota border. Color scheme and graphical components are as described in the caption of Fig. 4 and the layout is the same as that of Fig. 5.

rendered the slab invisible to tomography did not destroy the discontinuity that is creating P to S conversions from this dipping horizon. In contrast, if taken at face value the tomography models all suggest the slab disaggregates at depths below about 300 km into a set of fragments. The variance in defining the actual shape of disaggregated slab fragments in Fig. 7, however, implies that a simple model of a continuous slab to a point near the eastern edge of the Rocky Mountains in Montana cannot be rejected. Upper mantle structure in this region is best characterized as being very three-dimensional, likely representing the superposition of a long chain of tectonic processes over the past 200 Ma. Capturing the full geometry here is difficult, as the structure in the vicinity of this section seems to be the most three-dimensional of the sections illustrated. This example drives home a principle we want to reiterate. The best way to assess the features we describe is to load all 12 of the 3D volumes available in the supplement into a 3D visualization package, and to explore and evaluate them together.

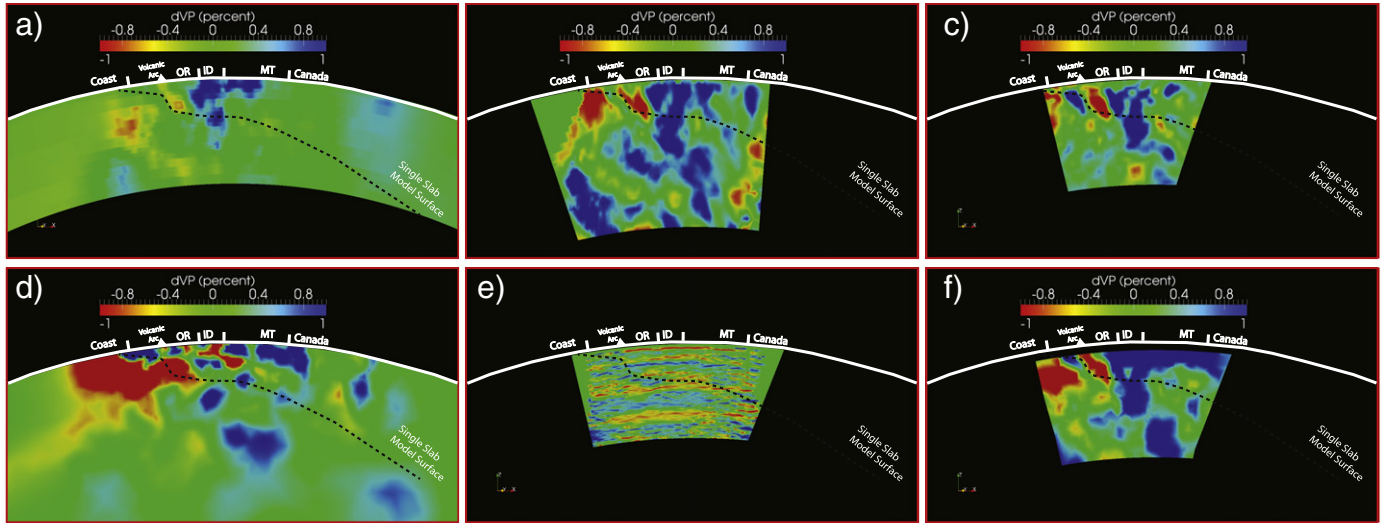
Although the tomographic results are in strong agreement on the presence of this “slab gap”, the interpretation of what process created the gap is not established. Obrebski et al. (2010) applied the model of Xue and Allen (2007) to argue that the slab disappears due to

interaction with warmer upper mantle material linked to the Yellowstone hotspot. They argue an upwelling heated the slab, removing the thermal anomaly that makes it visible elsewhere in these models. This might be called the “blowtorch model” for the slab gap.

Sigloch (2011) argues that the slab gap is more pervasive. This viewpoint comes from the broader perspective provided by her model as compared to regional models like Obrebski et al. (2010). Sigloch (2011) states this slab gap “is a major SW–NE trending fracture in the Cascadia system, striking from near the trench in southern Oregon into the lower mantle under the U.S.–Canadian border around 255° W”. Due to the difficulty of illustrating this three-dimensional feature we simply state that both of the other two larger scale models (MIT11 and TIA10) support this element of the Farallon slab geometry. We caution, however, that this observation is based on parts of these models constrained only by the much sparser coverage outside the USArray. In any case, Sigloch (2011) argues that this divide in the slab is much older and extends to a depth of 1100 km. Although the Oregon slab gap is consistent with the blowtorch model of Xue and Allen (2007), the observed gap in the deeper mantle in Canada is harder to explain since the kinematic model of Fig. 2 shows that that part of the slab is older than 40 Ma. Future work is needed to

Section DD'

P-wave Models



S-wave Models

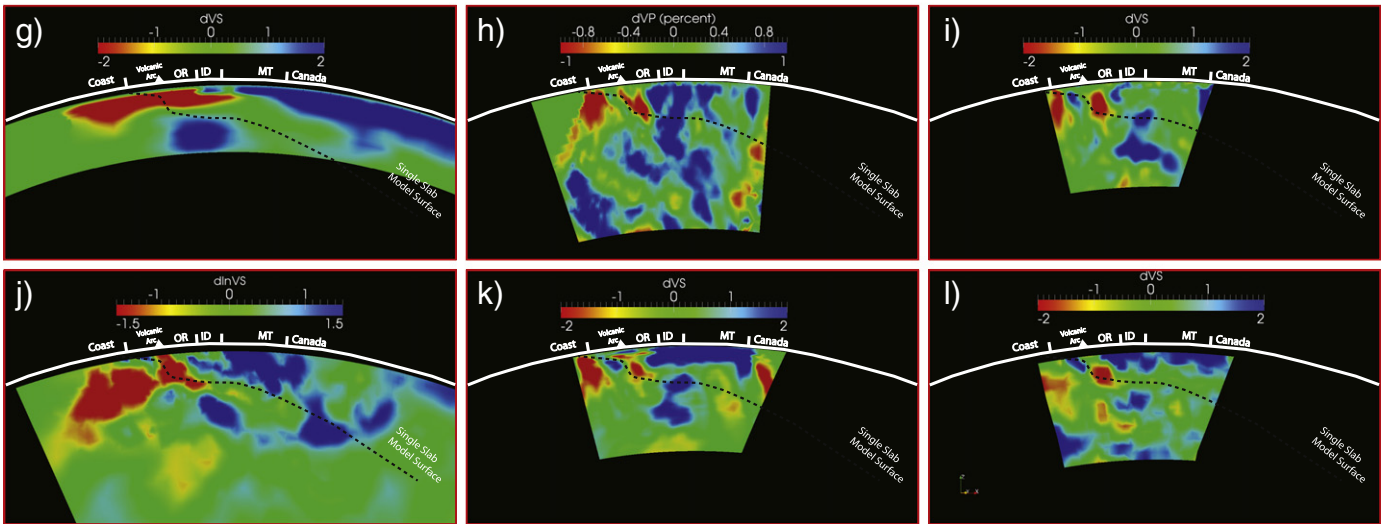


Fig. 7. Section DD' – southern Oregon to Winnipeg. Color scheme and graphical components are as described in the caption of Fig. 4 and the layout is the same as that of Fig. 5.

resolve what process created this larger scale slab gap. We suggest that this feature may be linked to an ancient slab window created by the now completely consumed Farallon–Kula ridge or the more controversial Resurrection plate of [Haeussler et al. \(2003\)](#). We suggest that more sophisticated three-dimensional modeling could be an opportunity to remove some of the ambiguity in defining the original geometry of the Kula.

4.2.3. Slab geometry under Washington State

Fig. 8 shows our northernmost cross-sections. Though located near the boundaries of a number of the tomography models the results are fairly consistent in defining the overall geometry in this region. West of the volcanic arc most of these results have insufficient resolution to resolve the gently dipping part of the Juan de Fuca plate that must connect the trench to the volcanic arc at a nominal depth of 100 km. The best wavespeed resolution in this depth range is provided by the combined surface-body wave inversion method of [Obrebski et al. \(2011\)](#). Their results (Fig. 8k) show a high velocity anomaly associated with this shallow slab that is not as clearly resolved in any of the other models. In addition, resolution of the top of the slab with receiver functions ([Li and Nabelek, 1999](#); [Nabelek et al., 1993](#)) was one of the early successes of the common conversion

point (CCP) stacking method. The algorithm used to generate PWMIG11 is, in some respects, a generalization of the CCP method, capable of resolving dipping horizons with lower station density, like that of the Transportable Array. A zoom into the converted wave image volume, in fact, shows the top of the slab along most of the subduction margin, although there are artifacts from irregular coverage provided by the EARS data. Later dense, linear profiles in other parts of Cascadia (see [Audet et al., 2010](#), for a current summary) indicate this is an unambiguous component of the subduction process.

The sections of Fig. 8 consistently indicate that the slab dip increases east of the volcanic front and remains steep down to at least the 410 km discontinuity. The dip in this section, however, is not nearly as steep as that linked to the Gorda plate (section CC', Fig. 6). What happens as the slab enters the transition zone, however, is less clear. Coverage decreases as the section passes beneath the Canadian border, from the dense USArray to the sparse and irregular Canadian and global seismic network stations. The only models in this collection that even cover this region are MIT11, SIG11, and TIA10 and the much lower resolution NA07 model. Both the SIG11 and TIA10 models indicate that the slab bends slightly at the top of the transition zone before descending at about the same angle (when viewed in

Section EE'

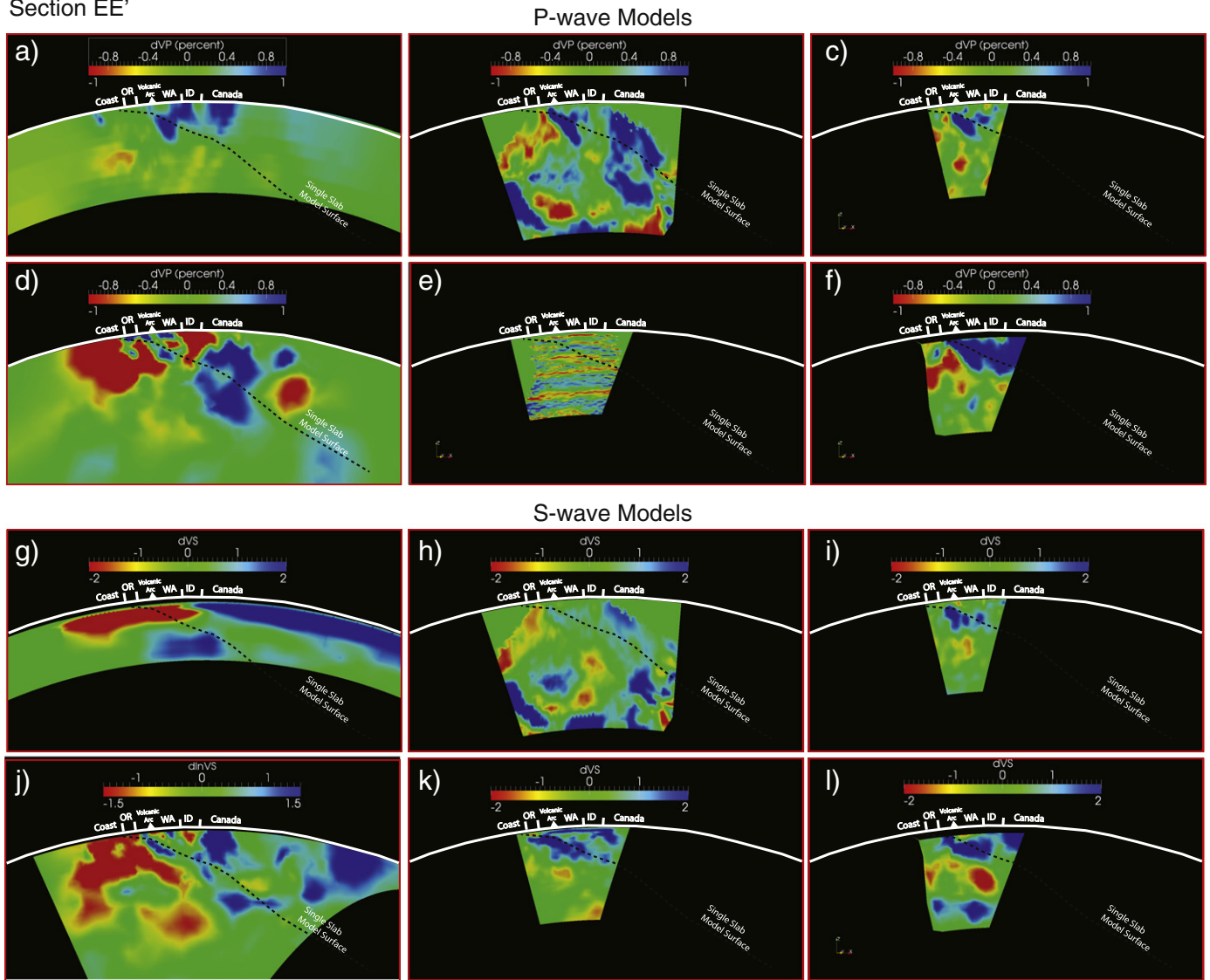


Fig. 8. Section EE' — northern Oregon to Saskatchewan. Color scheme and graphical components are as described in the caption of Fig. 4 and the layout is the same as that of Fig. 5.

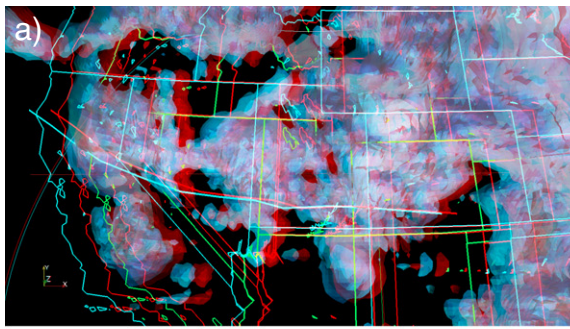
true 3D perspective as seen here) into the lower mantle. A positive velocity anomaly, consistent with a slab, is a feature of most of the models to at least the base of the transition zone. At deeper depths, the interpretation becomes more ambiguous because we pass into the region of the larger scale “slab gap” discussed in Section 4.2.2. Fig. 8d illustrates this gap as the near zero velocity anomaly (green) region between the fast body located in the transition zone near the Canadian border and the fast (blue) area in the lower right corner. Sigloch (2011) calls the latter the “old Farallon”. The single surface slab model shows that a simple surface is a reasonable geometry to

connect these two features, but the tectonic interpretation of this northern slab gap remains enigmatic.

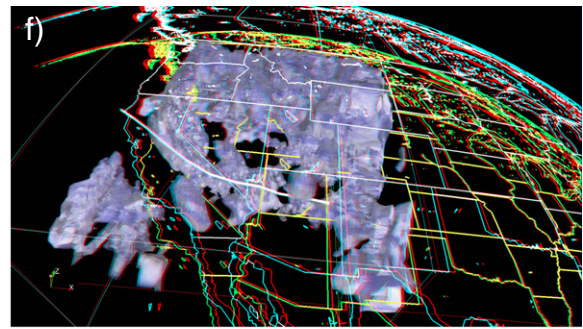
4.2.4. Slab window east of the San Andreas

Fig. 1 shows a map projection of edge of the slab window created by the opening of the San Andreas that is predicted by our model. The model we use here can be viewed as a refined version of that shown in Fig. 5 of Dickinson and Snyder (1979a). South of this curve the kinematic model predicts that the upper mantle should be slab-free. Fig. 9 displays this same curve in three-dimensions with a volume

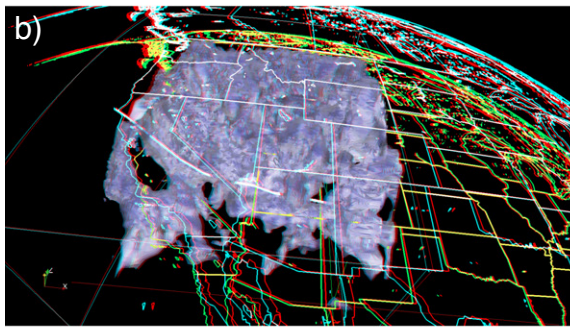
Fig. 9. Three-dimensional geometry of Mendocino slab window. These figures are stereo pair images that require a pair of anaglyph glasses to be seen in the three-dimensional geometry the figures display. Geographic and depth perspective is provided by coastline and political line data. The white geographic data is rendered at sea level and the yellow geographic data are projected to a depth of 400 km. The bold white curve cutting across the volume from Cape Mendocino to the Oklahoma panhandle is a three-dimensional rendering of the updip limit of the Farallon slab predicted from the model described in the text. It is three-dimensional rendering of the same curve plotted in map view in Fig. 1. Each figure displays the geometry of 10 of the 12 three-dimensional volumes compared in this paper. The first 5 are P wave models: (a) MIT11, (b) NWUS11-P, (c) DNA09P, (d) SIG11, and (e) UOP. The others are S wave models: (f) NWUS11-S, (g) DNA09S, (h) DNA10, (i) TIA10, and (j) UOS. The models are represented with three-dimensional isosurfaces rendered translucent to provide a form of volume visualization that works in anaglyph stereo. All use isosurface contours from 0.2% velocity perturbation upward to the maximum value at intervals of 0.1%. Note this implies negative velocity anomaly regions are made transparent so only positive anomalies are visible. The focus of this figure is the slab window linked to the Mendocino triple junction. To provide an unobstructed view of this part of the volume the viewpoint is variable for different models and some of the volumes had to be clipped in the radial direction. The clipping masks used are: (d) model is transparent above 60 km; (b),(e), (f), and (j), are transparent below 650 km; (c) and (g) are transparent below 600 km; and (h) is transparent below 700 km.



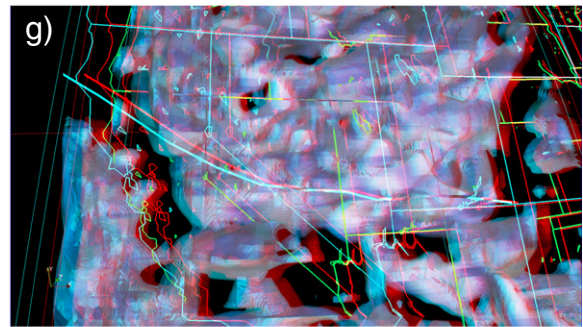
Burdick et al (2011)



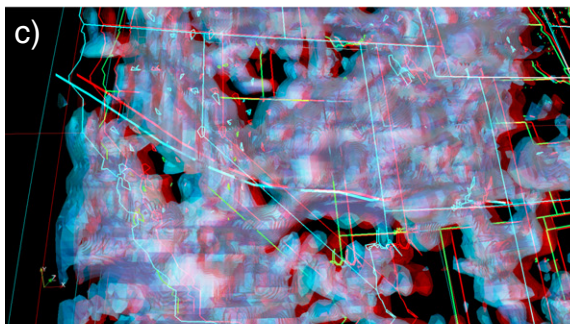
James et al. (2011) P model



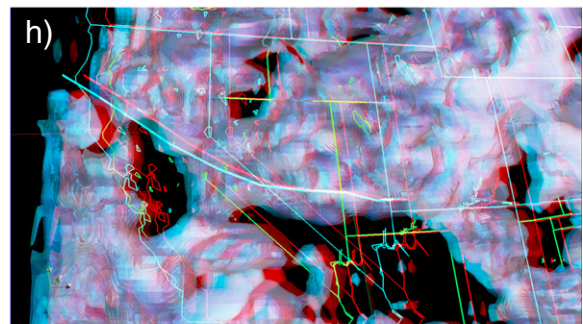
James et al. (2011) P model



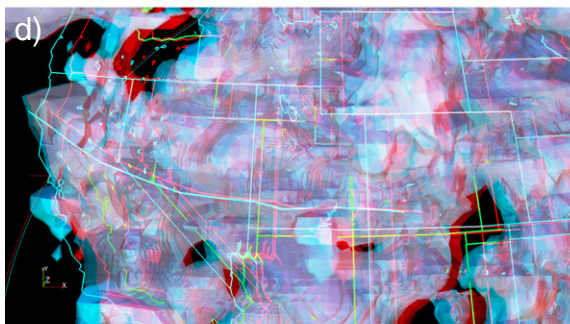
Obrebski et al. (2010) S model



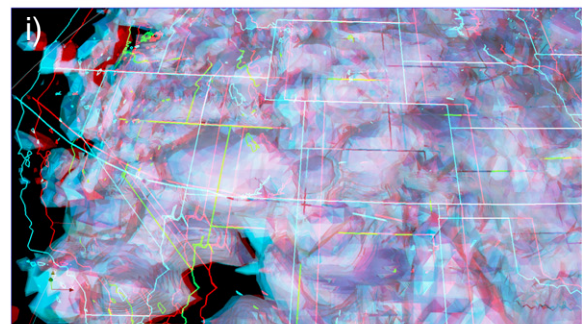
Obrebski et al. (2010) P model



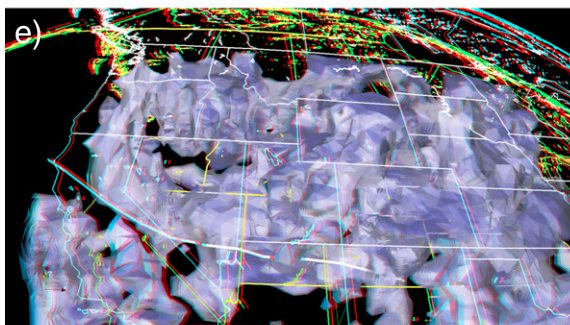
Obrebski et al. (2011)



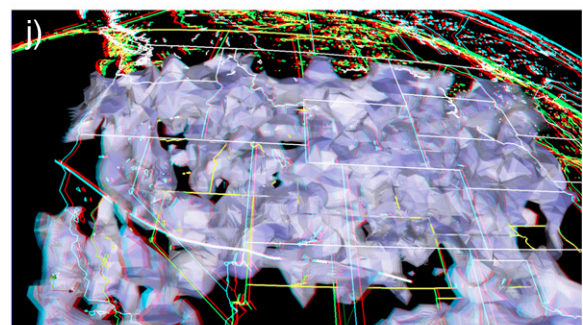
Sigloch (2011)



Tian et al. (2010)



Schmandt and Humphreys (2010) P model



Schmandt and Humphreys (2010) S model

visualization of 10 of the 11 tomography models we compare in this paper. The [Bedle and van der Lee \(2009\)](#) model is not shown because it has insufficient resolution at the relevant depths. The PWMIG11 result is not shown because the type of visualization used in [Fig. 9](#) is not effective on this type of image. The cross-sections in [Figs. 4e, 5e, and 6e](#) provide related perspectives to [Fig. 9](#).

Given that none of tomography models have a nominal resolution better than 100 km and considering the approximation used to generate the single surface slab model, the fit of the predicted edge of the slab window to all of the tomography models is striking. In all the models one can see the steeply dipping section of the slab in the west flattening under southern Oregon and Idaho. All models agree that, towards the south, the flat section vanishes in the vicinity of the predicted edge of the slab window, leaving a slab-free hole under most of California and Nevada. The agreement of the tomography models with the predictions of this simple kinematic model suggest this can be used to provide a strong constraint on geodynamic models of this western US. The excellent fit of predicted and observed slab window edges, from Cape Mendocino to Oklahoma, implies there has been no large north–south component of “mantle wind” to displace the slab. It also provides a strong, independent cross-validation of the Farallon–North America–Pacific plate model of [Dobrovine and Tarduno \(2008\)](#) up till at least 40 Ma. Either that or there is a coincidental canceling of errors.

[Fig. 5](#) shows another important point about the subduction geometry. This section crosses through an upper mantle velocity anomaly that has come to be called the southern Sierra drip ([Zandt et al., 2004](#)). [Jones et al. \(1994\)](#) first proposed this feature using data from an early IRIS-PASSCAL experiment. It was illuminated in more detail using data recorded by the Sierra Nevada EarthScope Project (SNEP), an early Flexible Array experiment ([Zandt et al., 2004](#)). It has been interpreted as lithospheric delamination related to the foundering of dense, upper mantle lithosphere linked to the Sierra Nevada batholiths ([Ruppert et al., 1998](#); [Zandt and Carrigan, 1993](#); [Zandt et al., 2004](#)). [Fig. 5](#), however, suggests an alternative explanation. This anomaly is located on the updip projection of the slab window. The spatial association suggests this “drip” could alternatively be viewed as a remnant of the Farallon plate torn away during the passage of the triple junction. Thus we suggest that geodynamic models of the Southern Sierra Drip should consider this element of the history as an alternative or at least a component of a delamination model.

4.3. Tests of regional scale results

4.3.1. Great Basin drip model

One of the first body wave tomography results from the USArray was that of [Roth et al. \(2008\)](#), which was the predecessor of NWUS11-P and NWUS11-S. In a companion paper [West et al. \(2009\)](#) proposed the idea of a lithospheric drip beneath the Great Basin based on a synthesis of the tomography data with shear wave splitting data, heat flow data, and volcanic history. They observed that these complementary data define a bull's-eye pattern centered on the top of a high wavespeed anomaly in the upper mantle revealed by the Roth et al. tomography result. They developed a numerical Rayleigh–Taylor instability drip model to explain the observations.

[Fig. 10](#) shows cross-sections through this feature in the same locations as [Fig. 2](#) of [West et al. \(2009\)](#). [Figs. 5, 6, and 9](#) are related views that provide a broader perspective on this feature. We suggest two key points can be gleaned from these three figures when compared to [Fig. 2](#) of [West et al. \(2009\)](#):

1. Although many details differ, the tomography models are generally in agreement that a strong positive velocity anomaly underlies a strong, pervasive, low-velocity zone throughout the entire Great Basin. The transition occurs between 100 and 300 km, depending on the model.

2. Viewed in the light of [Fig. 9](#) it seems clear this feature is not necessarily an isolated lithospheric fragment. An alternative suggested by [Fig. 9](#) is that it is linked to the well-resolved Farallon slab remnant described above. [Figs. 5, 6, and 9](#) show that the updip end of this feature is consistent with the slab window edge predicted from our single surface slab model.

These observations suggest an alternative interpretation of the [West et al. \(2009\)](#) paper. That is, the downwelling model used by West et al. to explain the shear wave splitting data is likely correct in concept, but the force driving the downwelling may be related to the larger scale Farallon subduction. The close association of this feature with the Mendocino slab window ([Fig. 9](#)) suggests that the downwelling region may be a smaller-scale component of the Mendocino slab window, rather than an independent block of material sinking into the mantle. Additional modeling work and new data are needed to explore the combined implications of the Mendocino slab model and the shear wave splitting results, and the volcanic history that formed the basis for the [West et al. \(2009\)](#) model.

4.3.2. Idaho/Oregon high velocity anomaly

[Schmandt and Humphreys \(2010b\)](#) introduced a novel interpretation of a high velocity body illuminated by several of the tomography models (e.g., [James et al., 2011](#); [Roth et al., 2008](#); [Schmandt and Humphreys, 2010a](#)). [Fig. 11](#) was constructed to evaluate the robustness of this feature. The approach used is the same as [Fig. 10](#). In this case the sections shown are directly comparable to [Fig. 2](#) of [Schmandt and Humphreys \(2011\)](#). We again show an extended section to evaluate the broader context possible with some of the other models and use 3D glyphs to mark the corners of the section displayed in the original paper. Section 10a, 10b, 10c, 10f, 10h, 10i, and 10k all show evidence of the west-dipping, high velocity body that [Schmandt and Humphreys \(2011\)](#) interpret as a relic slab suspended in the mantle after accretion of the Siletzia block. Furthermore, the scattered wave image in [Fig. 10e](#) corroborates the observation by [Eagar et al. \(2010\)](#) of elevation of the 410 km discontinuity in the vicinity of this feature with no related deflection of the 660 km discontinuity. The PWMIG11 image ([Fig. 11e](#)) also shows a series of west dipping, positive conversion horizon running from just above the 410 km discontinuity near the Idaho–Oregon border to eastern Montana. What these discontinuities represent is not known, but we note that this is the only area in the entire western U.S. where west-dipping conversions are observed in this depth range and downdip position relative to the trench.

We also note that the SIG11, the TIA10, and the UO10S model do not show this feature unambiguously. Furthermore, if one examines this feature with other 3D visualization techniques that are more challenging to present in print (volume visualization and/or 3D iso-surfaces like [Figs. 9 and 12](#)) one finds the detailed shape of this high velocity anomaly is very different for the different tomography models. The west dip and general extent defined in [Schmandt and Humphreys's \(2010b\)](#) paper, however, does appear to be reasonably robust. Thus we conclude that the general concept of a west-dipping, high velocity body in the upper mantle beneath the Idaho panhandle and eastern Oregon is reasonably well supported by the existing results.

4.4. Larger scale subduction geometry

4.4.1. Overview

Results on the lower mantle are more limited. Only SIG11, TIA10, and MIT11 are suitable for this purpose. The other tomography models are all limited to the western U.S. This difference results from a variation in the roots of the methods used by these groups. The models produced by [Burdick et al. \(2008, 2009, 2010\)](#) (MIT11) evolved from the global tomography method of [Li et al. \(2008\)](#)

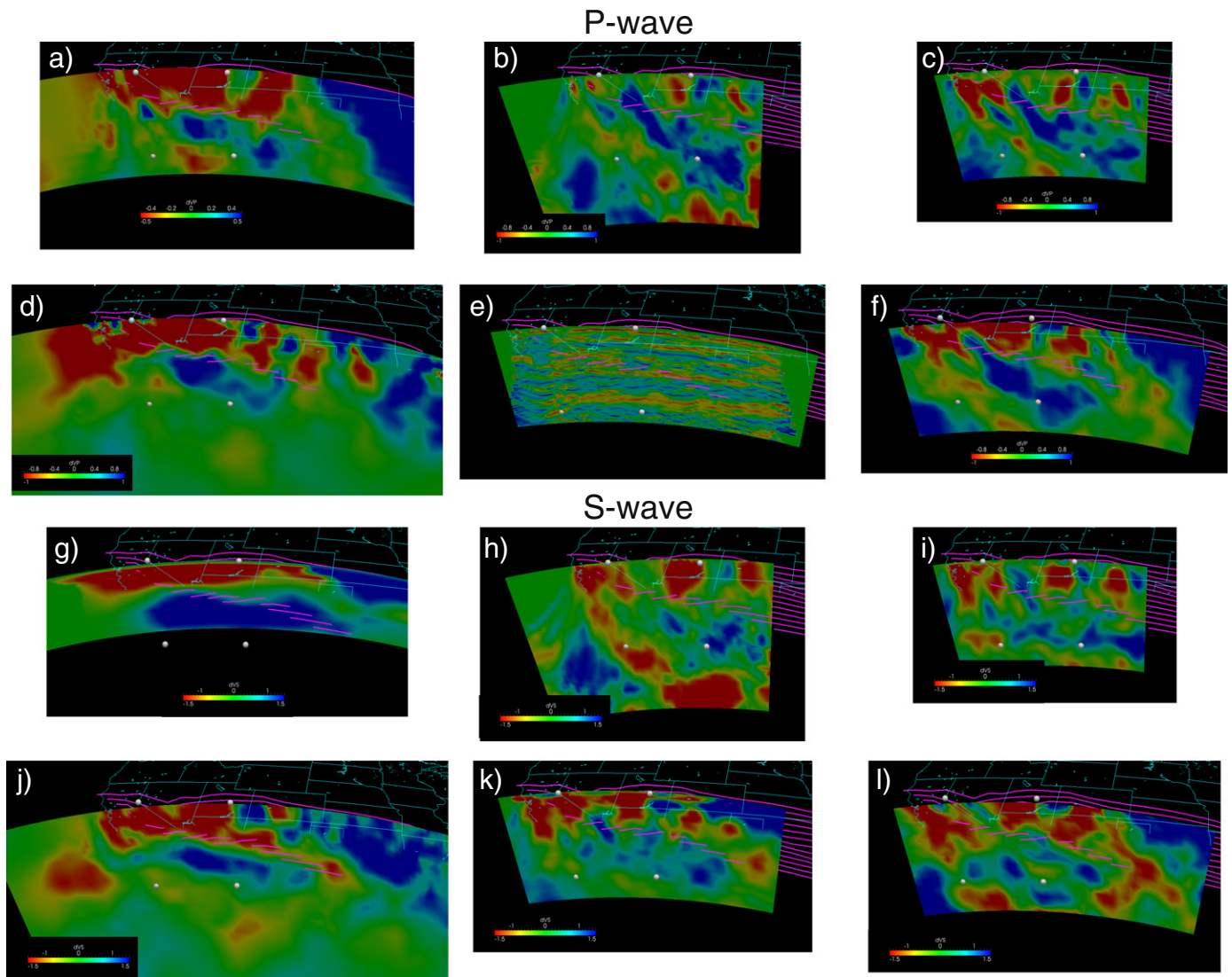


Fig. 10. East–west cross section congruent with Fig. 2c of West et al. (2009). Figure is a 3D projection with a viewpoint south and above the surface of the earth. Coastline data, major rivers, and political boundaries are displayed in their surface positions as cyan curves. The layout order of the sections is the same as that of Figs. 5–8. The white spheres are the corners of the section displayed in Fig. 2c of West et al. (2009). The magenta lines are the flow lines illustrated in the base map of Fig. 1 but seen here in a three-dimensional projection. A rainbow color map is used for all the figures, but unlike that of Figs. 4–8 the scaling varies for different sections to compensate for variations in overall amplitude between different models.

while SIG11 and TIA10 evolved from the global method by Montelli et al. (2004). All the others have roots in regional scale tomography methods and make a fundamental, often unstated assumption that structure in the lower mantle can be neglected or at least absorbed into a simple static (origin time correction) term. Most use tunable static corrections (station corrections) to reduce the impact of unresolved crustal structure. It is far from clear that either of these assumptions is valid. A hint that uncorrected global-scale anomalies are a problem with the regional models is in a detail of Fig. 9. It was necessary to mask the model results below the transition zone in several of these models. That was necessary because these models had positive velocity perturbations for a large fraction of the volume below the transition zone. We applied the mask in Fig. 9 purely to enhance the graphics. However, since the larger scale models have some complexity in the lower mantle of the western US, we suspect that the regional models may all contain artifacts of some degree created by structure outside the study volume.

In any case it is important to note that there is a large drop in the resolving power of SIG11, TIA10, and MIT11 outside of the Cordillera. This is an inevitable consequence of the transition from the very

dense station geometry of the USArray relative to the much sparser global coverage. A more subtle consequence is that the more irregular coverage outside the Cordillera leads to more irregular point resolution functions. An example is the output of a standard “checkerboard test” illustrated in Fig. 5 of Sigloch (2011). The figure demonstrates that in most regions outside the USArray, resolution irregularities cause the checkerboard output to be smeared in irregular ways. This distorts the output of all tomographic models in ways that are not possible to appraise by the pure visualization methods we are using here. All methods aim to reduce artifacts as much as technically possible, but where coverage is variable one has to always remember a basic axiom from inverse theory found in Lanczos (1961): no amount of mathematical trickery can correct for a fundamental lack of information. The point is that outside the area of USArray, the effective resolving power of the data is drastically lower and interpretation of the models therefore needs to be approached more cautiously.

4.4.2. The old Farallon slab in the lower mantle

The most robust anomaly in the lower mantle is the feature Sigloch (2011) calls the “old Farallon”. This is seen in Fig. 12 as the

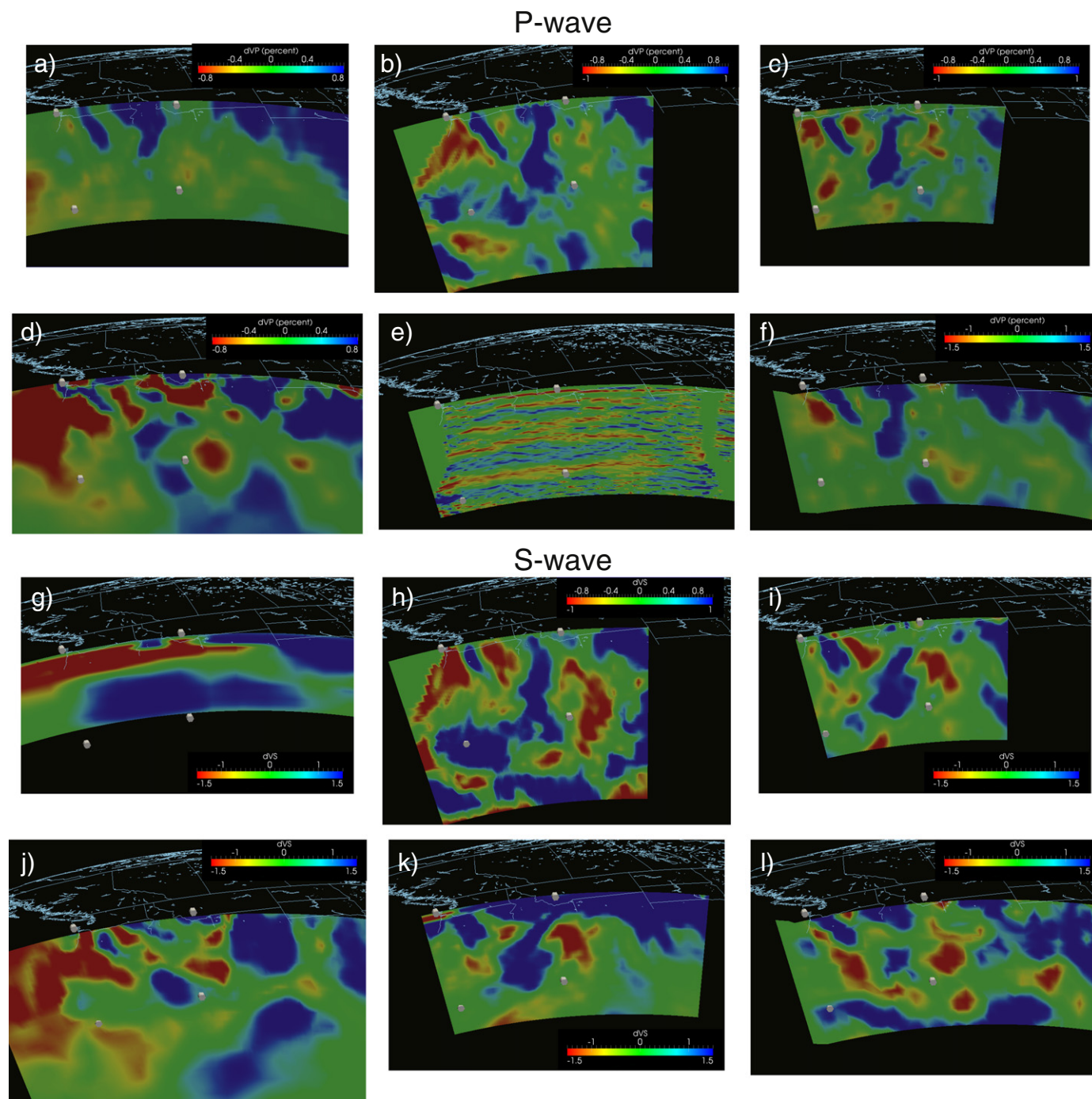


Fig. 11. Cross-sections congruent with that of Fig. 2 of Schmandt and Humphreys (2010b). The format of this figure is comparable to that of Fig. 10 except here the corners of the section use a cylindrical glyph and we do not display the flow lines for the single surface slab.

large, continuous, high-velocity body in the lower mantle under all of the eastern U.S. and Canada. The agreement in the overall geometry of the old Farallon revealed in these three models is strong. This can be seen more completely by viewing Animations 1–3 in the electronic supplement for this paper. This fast anomaly is not new as it has been a robust component of global tomography models since the original discovery by Grand (1994). We conclude that any model of the Farallon system must account for the presence of this large, robust feature of the lower mantle of North America.

Existing plate models of the Farallon plate are unambiguous in claiming that subduction of this plate has been a key geologic process shaping North America for more than 100 Myr. Perhaps the strongest

argument that this anomaly is linked to the “old Farallon” is its continuity. Although the Cenozoic history is complicated by a history of ridge subduction and related fragmentation of the plate, the Mesozoic history is comparatively simple. The prevailing model is that throughout most of the Mesozoic the entire western margin of North America was dominated by subduction of the Farallon and Kula plates. The clearest support for this statement is that this is the model commonly taught in introductory geology courses. An example is animations developed by Atwater found at http://emvc.geol.ucsb.edu/2_infopgs/IP3RegTect/dNoPacfic.html. A simple summary is that a reasonable perspective on the “old Farallon” is that it is the grave of the Farallon slab from the Mesozoic.

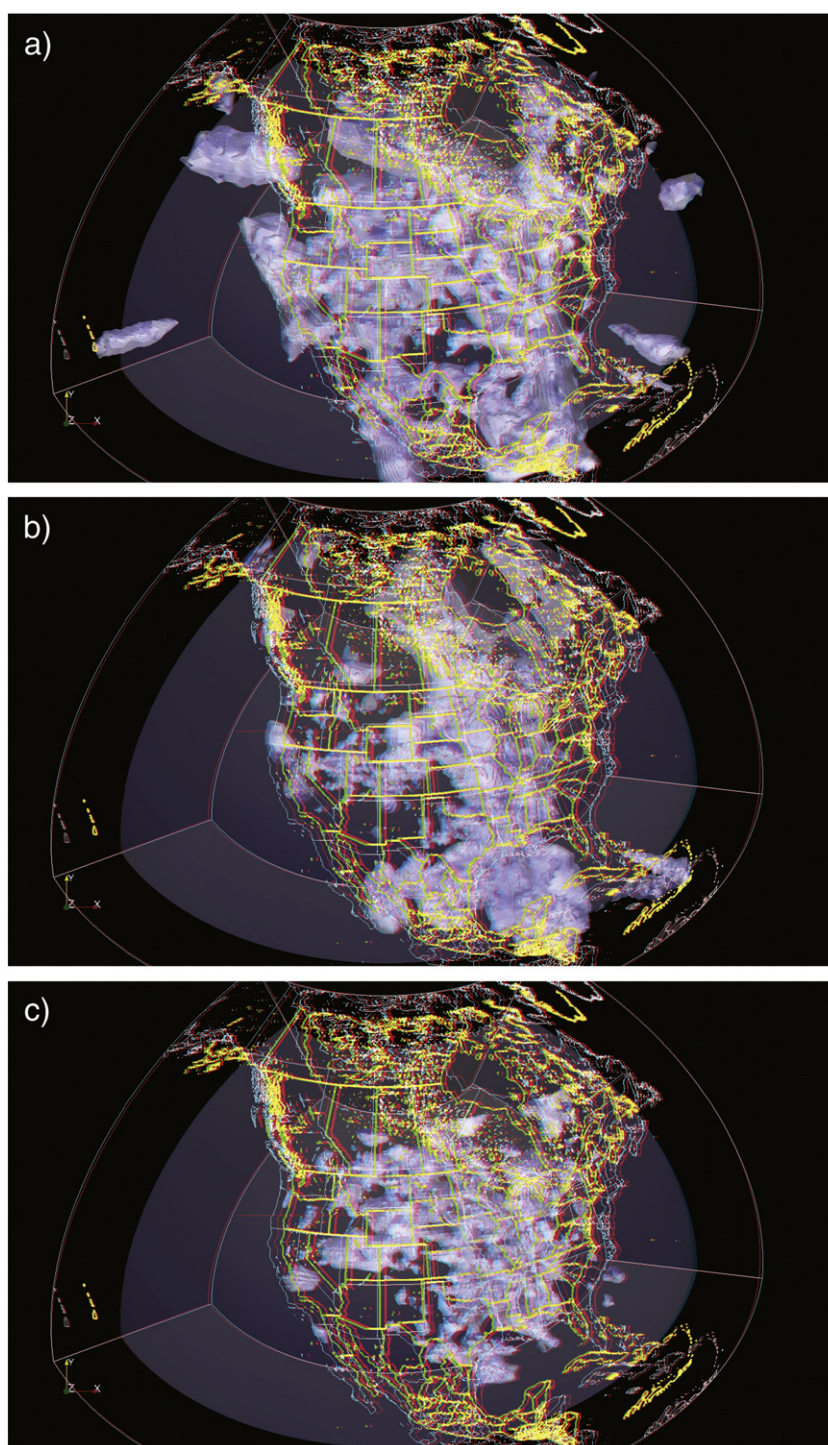


Fig. 12. Three-dimensional visualization of deeper geometry of the Farallon slab. This figure is a set of stereo pair images that requires a pair of anaglyph glasses to be viewed in stereo. The view is from radially above North America and illustrates the true three-dimensional geometry of three models (see Table 1): (a) SIG11, (b) MIT11, and (c) TIA10. The models are represented here by translucent isosurfaces as in Fig. 9 drawn from +0.4 to +1.4% by intervals of 0.2%. The objective of this figure is to illustrate the geometry of the deeper part of the mantle imaged by these models so the isosurface contours are clipped to display only isosurfaces at depths below 400 km. The components of this figure are frame 1 of flyby movies of this scene that are available in the electronic supplement.

4.4.3. The big break and the Farallon slab beneath the High Plains

Sigloch et al. (2008) were the first to describe a feature they dubbed “the big break” seen clearly in all three of the models shown in Fig. 12. The “big break” is a division line in the upper mantle beneath the High Plains, running from around the Nebraska–Kansas border south through Texas. It separates a transition zone filled with slab (to the northeast) from a neutral (slab-free) upper mantle

(to the southwest). With the visualization method used in Fig. 12 the slab-free area appears as a hole in the visible object under this region. A related element is the higher wavespeeds seen in the northern High Plains (Nebraska and the Dakotas) around the depth of the transition zone. Thus the “big break” runs only to around the geographic center of the lower 48 states. An important conclusion from this paper is that the three models shown in Fig. 12 all detect a large-

scale feature consistent with the “big break” geometry described by Sigloch (2011). Because all were produced from different data, and since this feature is huge, it is almost certainly a real element of North American geology.

A different question is a tectonic model for the origin of the “big break”. Sigloch et al. (2008) describe a model linked to a jump and tearing process of the Farallon slab that was hypothesized to occur in late Laramide time when the slab transitioned from a flat slab geometry to something closer to the present geometry. This was expanded in Sigloch (2011) where the high wavespeed anomaly in the northern high plains was linked to a stagnant slab suspended in the transition zone.

Results in this paper suggest an alternative hypothesis that needs to be explored further. The success of the 3D model we developed from Doubrovine and Tarduno's (2008) plate model in predicting the Mendocino slab window (Fig. 9) puts some strong constraints on the space-time location of the “big break”. If the “big break” is linked to Laramide subduction, there is a huge inconsistency with the time lines for the kinematic model shown in Figs. 1–3. The slab would have had to undergo a compression of nearly 100% to move even the 50 Ma contour to the western edge of the “big break”. This is not inconceivable, but Figs. 1–3 suggests an alternative hypothesis. If you accept the time-line on the slab window shown in Fig. 1, the intersection of the slab window curve with the one defining the “big break” occurs at approximately the time of initial ridge subduction near the modern Gulf of California. The flow lines from intersection point project to a point a few hundred kilometers north of the current Pacific–North America–Cocos triple junction. Thus the “big break” may be linked the San Andreas slab window. There are, however, complexities we are not modeling properly related to the opening of the Gulf of California during the past 5–10 Ma (e.g. Lonsdale, 1989) and the related southward progression of the Cocos–North America–Pacific triple junction.

5. Discussion and conclusions

Modern models of plate tectonics require that the mantle under North America had to have been profoundly influenced by the subduction of the Farallon and Kula plates. The set of models we compared in this paper show that this is indeed the case and that all the results we examine show elements consistent with this zeroth-order assumption. An initial reaction anyone is likely to have, however, is that the models are disturbingly different. Previous experience with comparison of seismic velocity inversion in active source experiments (Zelt, 1999) and global tomography (e.g. Becker and Boschi, 2002), however, indicated similar issues. The reason for this is a generic weakness in current generation seismic tomography methods. Seismic tomography images differ in a fundamental way from images produced by similar technical methods in medical imaging. Medical imaging devices are carefully engineered to make coverage and illumination as uniform as possible and the inversion algorithm that is used is fixed for a given device. Passive seismic array imaging methods are all at the mercy of where earthquakes happened to occur during the time of deployment. This creates irregularities that all methods aim to suppress, but which inverse theory shows are fundamentally impossible to remove completely. In a comparison like this, we have the added complexity of variations in how the inversion is regularized, and even the mix of data and assumptions of the method. As a result, those familiar with inverse theory in general and seismic tomography in particular should not be surprised by the divergence of the results.

A fundamental problem this exercise demonstrates is that seismic tomography has come to be viewed too much as a turnkey method. We assert that far more emphasis needs to be devoted to error appraisal of models than what is the norm today. Evidence for our collective guilt on this problem is that none of us who have distributed

tomography models to the community provide any kind of error metrics on the models in electronic form. If we are to make full use of the large investment made in USArray, the community needs to develop methods to more objectively evaluate and/or compare models like this.

Lacking effective tools for quantitative comparison of these tomography models, we appealed here to a graphical approach using modern three-dimensional visualization methods. A summary of the geometry we argue can be inferred from the existing results follows, organized from west to east.

1. The remnant of the Farallon plate is the Juan de Fuca/Gorda plate. Evidence from receiver function profiles (Audet et al., 2010) along this margin indicate unambiguously that the slab dips gently in a normal subduction system to intersect the Cascadia volcanic arc at a depth within the range of other subduction zones around the globe reviewed by England et al. (2004).
2. The tomography models all indicate that the dip of the slab steepens sharply at the volcanic arc along the entire margin. Note that this was not known unambiguously prior to USArray because the slab does not seem to generate earthquakes deeper than 100 km.
3. The dynamics of the subducting plate seems to be strongly influenced by the 410 km discontinuity along the entire margin. The results are in general agreement that the slab flattens everywhere immediately above the 410 km discontinuity. In Oregon and northern Nevada the slab curves sharply from a steep dip to a more gentle dip. Scattered wave image results provide a high-resolution interpretation for the top of the slab between depths of approximately 300 km to the top of the 410 km discontinuity (Pavlis, 2011b). In the transition zone and below, the slab becomes more transparent and no comparable discontinuity has been detected that can be correlated with the tomography models.
4. The geometry of the Farallon slab is unambiguously three-dimensional. Probably the most important outcome of this paper is a clarification of the geometry of the southern edge of the slab, which is intimately related to the slab window created by the northward motion of the Cape Mendocino triple junction. We argue that the synthesis of the tomography models shown in Fig. 9 provide strong evidence that the southern edge of the Farallon slab is located close to the curve illustrated in map view in Fig. 1 and in three-dimensions in Figs. 3 and 9. The “Great Basin Drip” as interpreted by West et al. (2009) may actually be linked to kinematics generated by the Mendocino slab window. This feature thus may not be a parcel of upper plate lithosphere sinking into the mantle but rather a part of the much larger Farallon system. Similarly, we find the suggestion by Obrebski et al. (2010) that the slab is imbricated into two steeply dipping segments along the Oregon–Nevada border is a probably a misconception created by 2D thinking applied to this 4D problem. The Obrebski et al. (2010, 2011) models include what we suspect is an artifact that contributed to this misconception, but the fundamental problem is using mainly cross sections and horizontal slicing methods to visualize four-dimensional objects.
5. The geometry of the northern equivalent of the Mendocino slab window is more ambiguous. That is, the Mendocino slab window must have a mirror image in Canada created by the Juan de Fuca (Farallon)–Pacific–North America triple junction over the past 30 Ma. The USArray provides minimal constraints on this part of the system because the kinematics of the system demands that the comparable slab edge is defined by a trajectory running generally north-northeast from the termination of the Explorer ridge near the north end of Vancouver Island. What we can say is that in the 300–500 km depth range the subducting slab does seem to steepen under the state of Washington relative to the more gently dipping geometry seen in southeast Oregon and northern Nevada.

An important first order feature of the geology of North America is that the width of the orogenic belt decreases dramatically in Canada compared to the western U.S. The [Dobrovine and Tarduno \(2008\)](#) model flow lines are nearly orthogonal to the strike of the orogenic belt in Canada. Where this change in dip occurs correlates directly with a huge change in width of the orogenic belt measured along the direction of these flow lines. The change in dip of the subducting slab in the state of Washington is also linked to a complexity of the system highlighted by [Schmandt and Humphreys \(2011\)](#). The tomography models all illuminate the presence of a high velocity body in the top 400 km of the mantle roughly coincident with the panhandle of Idaho. This feature is also linked to an elevation of the 410 km discontinuity noted by [Eagar et al. \(2010\)](#) and confirmed by the plane wave migration image included with this paper. Schmandt and Humphreys interpret this feature as a relic of a westward jump in the position of the trench linked to the accretion of the Siletzia terrane at 55 Ma. In any case, this corner of the U.S. seems to have experienced an exceptionally complicated history that is not yet fully understood.

6. Closely associated in space and time with the Siletzia accretion model of [Schmandt and Humphreys \(2011\)](#) is the Snake River Plain–Yellowstone system. The tomography models are in strong agreement on at least one general statement: some process has caused the fast velocities that characterize the slab elsewhere in the western U.S. to vanish in the region under the erupted volcanics running from eastern Oregon to Yellowstone. Some version of the blowtorch model of [Xue and Allen \(2007\)](#) is one model for the process that created this robust feature. An alternative hypothesis (Humphrey, personal communication) is that this gap is created by a north–south extension of the slab created by the local “mantle wind”. Finally, a recently proposed hypothesis is that this feature is related to complex subduction of the Farallon ([James et al., 2011](#)), whereby the edge of the Juan de Fuca plate that lays subhorizontally beneath the Snake River Plain / Yellowstone system, guiding upward flow at the leading edge of the slab before it increases dip into the uppermost lower mantle. Numerical models of [Faccenna et al. \(2010\)](#), corroborate this style of subduction-induced mantle upwelling.
7. If we continue down dip (northeast) at around the 30 Ma contour in [Fig. 1](#), the Farallon slab seems to have completely passed into or through the transition zone. This feature of the geometry is seen in full context only in the larger scale models (SIG11, TIA10, and MIT11) because the USArray is in the process of passing over the relevant part of the mantle. A first order inference we can make today ([Fig. 12](#) and Animation 1 of the supplement) is that there is not a continuous, positive anomaly where it might be expected. Under the southern Great Plains the slab vanishes in what [Sigloch et al. \(2008\)](#) and [Sigloch \(2011\)](#) call the “big break”. A saddle of high velocity material is seen in the northern Great Plains, but a second swath of slab-free mantle is seen in the comparable position from near the Canadian border in North Dakota northward.
8. In the eastern U.S. and Canada the larger scale models all unambiguously image the deep Farallon slab originally discovered by [Grand \(1994\)](#). This is imaged as a strong, high velocity body in both P and S waves that forms a continuous body running from Northwest Territories of Canada to at least as far south as Cuba. Since its discovery this anomaly has been largely accepted as the grave of the old Farallon plate. The new results do nothing to dispel that model. The new results, however, are somewhat enigmatic at present in linking the high-resolution results in the western U.S. to the old Farallon. The geodynamic processes that led to the “big break” and the northern slab-free area discussed by [Sigloch \(2011\)](#) have not been completely established. This is likely to emerge as a topic of interest in the next few years because USArray is in the process of rolling over the key real estate.

We close by putting forward the following assertion: the geology literature is full of misconceptions and erroneous conclusions linked to 2D thinking applied to 4D problems. The current state of knowledge of the geometry of the Farallon/Kula plate is a perfect case in point. To really understand this system requires coordination between 4D geodynamic modeling and seismic imaging to test models with real data constraints. This paper illustrates an initial step in that direction. We use two tools that need to be put in the top drawer of every scientist working on USArray data: (1) a full featured, three-dimensional visualization system, and (2) tools to provide some form of quantitative 4D model of the geometry. The first is a well-developed technology today and feasible on any desktop computer. Publications have universally moved to electronic media and publishing 3D or 4D visualizations is no longer a barrier. The second is more of a suggestion for future work to sort out many of the remaining issues. The model we used here has a long string of assumptions, some of which are highly questionable. Nonetheless, any quantitative, 4D model is better than arm waving arguments that are untestable. A case in point is that although the model we use is simple, it is remarkably successful in predicting the geometry of edge of the slab that defines the Mendocino slab window. We hope this demonstrates the promise of using even simple 4D models as constraints on the system.

6. Electronic supplement

Available from this URL: <https://scholarworks.iu.edu/dspace/handle/2022/14164>.

6.1. Animations

The files sig11.mov, mit11.mov, and tianetal.mov are moving camera animations that are extensions of [Fig. 12a, b, and c](#) respectively. [Fig. 12](#), in fact, is constructed from the first frame of each of these movies. The movies provide a broader context for these models than the static figure. See the caption of [Fig. 12](#) for an explanation of the elements of the scene.

6.2. Visualization files

One of the primary goals of this paper was to provide the community a set of data files that are referenced in a common coordinate system so they can be viewed together in true 3D geometry. For this reason we strongly urge all readers to download the supplement and install the open source package called paraview (<http://www.paraview.org>). The data files are a collection of graphical objects that can be viewed together as a 3D scene in paraview. See the README files in each directory for a description of each data file.

Numerous tutorials for paraview are now available on the web. Other visualization packages that support Visualization Tool Kit (VTK) formats may also be able to read these files directly since paraview has become a common visualization package.

Acknowledgments

We thank Brandon Schmandt and Gene Humphreys for sending us their models in electronic form. We also thank the other groups who provided their models electronically as a service to the community. Pavlis gives special thanks to Gene Humphrey for sharing some of his insights on this problem, to Rob Porritt for clarifying some details of the UCB tomography algorithms during the EarthScope Imaging Science Workshop, and Rob van der Hilst for many helpful suggestions as we were completing the paper. He also acknowledges work by Xin Liu in producing PWMIG11. We thank Pavel Dobrovine and an anonymous reviewer for constructive feedback that improved the paper significantly. The Transportable Array component of the USArray facility is a Major Research Facility supported by the National

Science Foundation under cooperative agreement EAR-0350030. Pavlis acknowledges support from the EarthScope program under award EAR-0951622. Fouch acknowledges support from the National Science Foundation under awards EAR-0548288 (EarthScope CAREER grant) and EAR-0507248 (Continental Dynamics High Lava Plains grant).

References

- Atwater, T., 1970. Implications of plate tectonics for Cenozoic tectonic evolution of western North America. *Geological Society of America Bulletin* 81, 3513–3536.
- Atwater, T., 1989. Plate tectonic history of the northeast Pacific and western North America. In: Winterer, E.L., Hussong, D.M., Decker, R.W. (Eds.), *The Eastern Pacific Ocean and Hawaii (The Geology of North America)*. Geological Society of America, Boulder, Colo, pp. 21–72.
- Audet, P., Bostock, M.G., Boyarko, D.C., Brudzinski, M.R., Allen, R.M., 2010. Slab morphology in the Cascadia fore arc and its relation to episodic tremor and slip. *Journal of Geophysical Research* 115, B00A16. doi:10.1029/2008JB006053.
- Basin, C., Laske, G., Masters, G., 2000. EOS Transactions. American Geophysical Union 81, F897.
- Becker, T.W., Boschi, L., 2002. A comparison of tomographic and geodynamic mantle models. *Geochemistry, Geophysics, Geosystems* 3. doi:10.1029/2001GC000168.
- Bedle, H., van der Lee, S., 2009. S velocity variations beneath North America. *Journal of Geophysical Research* 114, B07308. doi:10.1029/2008JB005949.
- Burdick, S., Li, C., Martynov, V., Cox, T., Eakins, J., Mulder, T., Astiz, L., Vernon, F.L., Pavlis, G.L., van der Hilst, R.D., 2008. Upper mantle heterogeneity beneath North America from travel time tomography with global and USArray Transportable Array data. *Seismological Research Letters* 79, 384–392.
- Burdick, S., Li, C., Martynov, V., Cox, T., Eakins, J., Mulder, T., Astiz, L., Vernon, F.L., Pavlis, G.L., van der Hilst, R.D., 2009. Model update December 2008; upper mantle heterogeneity beneath North America from P-wave travel time tomography with global and USArray transportable array data. *Seismological Research Letters* 80 (4), 638–645. doi:10.1785/gssrl.80.4.638.
- Burdick, S., van der Hilst, R.D., Vernon, F.L., Martynov, V., Cox, T., Eakins, J., Karasu, G., Teytel, J., Astiz, L., Pavlis, G.L., 2010. Model update January 2010; upper mantle heterogeneity beneath North America from P-wave travel time tomography with global and USArray transportable array data. *Seismological Research Letters* 81 (5), 689–693. doi:10.1785/gssrl.81.5.689.
- Crotwell, H.P., 2007. High data volume seismicology: surviving the avalanche. Ph.D. dissertation, Univ. of S. Carolina, Columbia, S.C., 86 p.
- Crotwell, H.P., Owens, T.J., 2005. Automated receiver function processing. *Seismological Research Letters* 76 (2), 702–709.
- Dahlen, F.A., Hung, S.H., Nolet, G., 2000. Fréchet kernels for finite-frequency traveltimes—I, theory. *Geophysical Journal International* 141, 157–174.
- Dickinson, W.R., Snyder, W.S., 1979a. The geometry of subducted slabs related to the San Andreas transform. *Journal of Geology* 87 (6), 609–627.
- Dickinson, W.R., Snyder, W.S., 1979b. Geometry of triple junctions related to San Andreas transform. *Journal of Geophysical Research* 84 (B2), 561–572.
- Dobrovine, P.V., Tarduno, J.A., 2008. A revised kinematic model for the relative motion between Pacific oceanic plates and North America since the Late Cretaceous. *Journal of Geophysical Research* 113, B12101. doi:10.1029/2008JB005585.
- Eagar, K.C., Fouch, M.J., James, D.E., 2010. Receiver function imaging of upper mantle complexity beneath the Pacific Northwest, United States. *Earth and Planetary Science Letters* 297, 141–153. doi:10.1016/j.epsl.2010.06.015.
- Engdahl, E.R., van der Hilst, R.D., Buland, R., 1998. Global teleseismic earthquake relocation with improved travel times and procedures for depth determination. *Bulletin of the Seismological Society of America* 88, 722–743.
- Engelbreton, D.C., Cox, A., Gordon, R.G., 1985. Relative motions between oceanic and continental plates in the Pacific basin. *Geological Society of America Special Paper* 206 (59 pp.).
- England, P., Engdahl, R., Thatcher, W., 2004. Systematic variations in the depth of slabs beneath arc volcanoes. *Geophysical Journal International* 156, 377–408.
- Faccenna, C., Becker, T., Lallemand, S., Lagabrielle, Y., Funicello, F., Piromallo, C., 2010. Subduction “plumes” in the upper mantle. *Earth and Planetary Science Letters* 299, 54–68.
- Grand, S.P., 1994. Mantle shear structure beneath the Americas and surrounding oceans. *Journal of Geophysical Research* 99 (B6), 11,591–11,621.
- Haeussler, P.J., Bradley, D.C., Wells, R.E., Miller, M.L., 2003. Life and death of the Resurrection plate: evidence for its existence and subduction in the northeastern Pacific in Paleocene–Eocene time. *Geological Society of America Bulletin* 115 (7), 867–880.
- James, D.E., Fouch, M.J., Carlson, R.W., Roth, J., 2011. Slab fragmentation, edge flow and the origin of the Yellowstone hotspot track. *Earth and Planetary Science Letters*. doi:10.1016/j.epsl.2011.09.007.
- Jones, C.H., Kanamori, H., Roecker, S.W., 1994. Missing roots and mantle “drips”: regional Pn and teleseismic arrival times in the southern Sierra Nevada and vicinity, California. *Journal of Geophysical Research* 99, 4567–4601.
- Kennett, B.L.N., Engdahl, E.R., Buland, R., 1995. Constraints on seismic velocity in the Earth from travel times. *Geophysical Journal International* 122, 108–124.
- Lanczos, C., 1961. *Linear Differential Operators*. Van Nostrand Reinhold, New York.
- Li, X., Nabelek, J.L., 1999. Deconvolution of teleseismic body waves for enhancing structure beneath a seismometer array. *Bulletin of the Seismological Society of America* 89, 190–201.
- Li, C., van der Hilst, R.D., Engdahl, E.R., Burdick, S., 2008. A new global model for P wave speed variations in Earth's mantle. *Geochemistry, Geophysics, Geosystems* 9, Q05018. doi:10.1029/2007GC001806.
- Lonsdale, P.F., 1989. Geology and tectonic history of the Gulf of California. In: Winterer, E.L., Hussong, D.M., Decker, R.W. (Eds.), *The Eastern Pacific Ocean and Hawaii (The Geology of North America)*. Geological Society of America, Boulder, Colo, pp. 499–521.
- Montelli, R., Nolet, G., Dahlen, F., Masters, G., Engdahl, E., Hung, S.-H., 2004. Global P and PP travel time tomography: rays vs. waves. *Geophysical Journal International* 158, 637–654.
- Nabelek, J., Li, X., Azevedo, S., Braunmiller, J., Fabritius, A., Leitner, B., Trehu, A., Zandt, G., 1993. A high-resolution image of the Cascadia subduction zone from teleseismic converted phases recorded by a broadband seismic array. *EOS Transactions of the American Geophysical Union* 74 (43) (Fall Meet. Suppl.), 431.
- Nettles, M., Dziewonski, A.M., 2008. Radially anisotropic shear velocity structure of the upper mantle globally and beneath North America. *Journal of Geophysical Research* 113, B02303. doi:10.1029/2006JB004819.
- Obrebski, M., Allen, R.M., Xue, M., Hung, S.-H., 2010. Slab–plume interaction beneath the Pacific Northwest. *Geophysical Research Letters* 37, L14305. doi:10.1029/2010GL043489.
- Obrebski, M., Allen, R.M., Pollitz, F., Hung, S.-H., 2011. Lithosphere–asthenosphere interaction beneath the western United States from the joint inversion of body-wave traveltimes and surface-wave phase velocities. *Geophysical Journal International* 185, 1003–1021. doi:10.1111/j.1365-246X.2011.04990.x.
- Pavlis, G.L., 2005. Direct imaging of the coda of teleseismic P waves. *Seismic Earth: Array Analysis of Broadband Seismograms*. AGU. Mono., 157, pp. 171–185.
- Pavlis, G.L., 2011a. Three-dimensional wavefield imaging of the codas of the USArray: new constraints on the geometry of the Farallon slab. *Geosphere* 7, 785–801.
- Pavlis, G.L., 2011b. Three-dimensional, wavefield imaging of broadband seismic array data. *Computers and Geosciences* 37, 1054–1066. doi:10.1016/j.cageo.2010.11.015.
- Pollitz, F.F., Snoko, J.A., 2010. Rayleigh-wave phase-velocity maps and three-dimensional shear velocity structure of the Western US from local non-plane surface wave tomography. *Geophysical Journal International* 180 (3), 1153–1169. doi:10.1111/j.1365-246X.2009.04441.x.
- Poppeliers, C., Pavlis, G.L., 2003a. Three-dimensional plane wave migration of teleseismic P-to-S converted phases: part 1, theory. *Journal of Geophysical Research* 108, 2112. doi:10.1029/2001JB000216.
- Poppeliers, C., Pavlis, G.L., 2003b. Three-dimensional plane wave migration of P-to-S converted phases: part 2, stacking multiple events. *Journal of Geophysical Research* 108, 2267. doi:10.1029/2001JB001583.
- Roth, J.B., Fouch, M.J., James, D.E., Carlson, R.W., 2008. Three-dimensional seismic velocity structure of the northwestern United States. *Geophysical Research Letters* 35, 1–4. doi:10.1029/2008GL034669.
- Ruppert, S., Flidner, M., Zandt, G., 1998. Thin crust and active upper mantle beneath the Southern Sierra Nevada in the western United States. *Tectonophysics* 286, 237–252.
- Schmandt, B., Humphreys, E., 2010a. Complex subduction and small-scale convection revealed by body-wave tomography of the western United States mantle. *Earth and Planetary Science Letters* 297, 435–445. doi:10.1016/j.epsl.2010.06.047.
- Schmandt, B., Humphreys, E., 2010b. Seismic heterogeneity and small-scale convection in the southern California upper mantle. *Geochemistry, Geophysics, Geosystems* 11, Q05004. doi:10.1029/2010GC003042.
- Schmandt, B., Humphreys, E., 2011. Seismically imaged relict slab from the 55 Ma Siletzia accretion to the northwest United States. *Geology* 39 (2), 175–178. doi:10.1130/G31558.1.
- Schroeder, W., Martin, K., Lorensen, B., 2006. *The Visualization Tool Kit: A Object-Oriented Approach to 3D Graphics*, 4th edition. Pearson Education, Columbia. (512 pp.).
- Sigloch, K., 2011. Mantle provinces under North America from multifrequency P wave tomography. *Geochemistry, Geophysics, Geosystems* 18 (2), Q02W08. doi:10.1029/2010GC003421.
- Sigloch, K., Nolet, G., 2006. Measuring finite-frequency body-wave amplitudes and traveltimes. *Geophysical Journal International* 167 (1), 271–287. doi:10.1111/j.1365-246X.2006.03116.x.
- Sigloch, K., McQuarrie, N., Nolet, G., 2008. Two-stage subduction history under North America inferred from multiple-frequency tomography. *Nature Geosciences* 1, 458–462. doi:10.1038/ngeo231.
- Tian, Y., Montelli, R., Nolet, G., Dahlen, F., 2007. Computing traveltime and amplitude sensitivity kernels in finite-frequency tomography. *Journal of Computational Physics* 226, 2271–2288.
- Tian, Y., Sigloch, K., Nolet, G., 2009. Multiple-frequency SH-wave tomography of the western U.S. upper mantle. *Geophysical Journal International* 178 (3), 1384–1402. doi:10.1111/j.1365-246X.2009.04225.x.
- Tian, Y., Zhou, Y., Sigloch, K., Nolet, G., Laske, G., 2011. Structure of North American mantle constrained by simultaneous inversion of multiple-frequency SH, SS, and Love waves. *Journal of Geophysical Research* 116, B02307. doi:10.1029/2010JB007704.
- van der Hilst, R.D., Wildyantor, S., Engdahl, E.R., 1997. Evidence for deep mantle circulation from global tomography. *Nature* 386, 578–584.
- van der Lee, S., Nolet, G., 1997. Upper mantle S velocity structure of North America. *Journal of Geophysical Research* 102 (10), 22,815–22,838.
- van der Lee, S., Frederiksen, A., 2005. Surface wave tomography applied to the North American upper mantle. In: Levander, A., Nolet, G. (Eds.), *Seismic Earth: Array analysis if broadband seismograms*, *Geophysical Monograph*, pp. 67–80.
- VanDecar, J. C., 1991. Upper-mantle structure of the Cascadia subduction zone from non-linear teleseismic travel-time inversion, Ph.D. dissertation, Univ. of Washington, Seattle, WA.

- VanDecar, J.C., Crosson, R.S., 1990. Determination of teleseismic relative phase arrival times using multi-channel cross-correlation and least squares. *Bulletin of the Seismological Society of America* 80 (1), 150–159.
- West, J.D., Fouch, M.J., Roth, J.B., Elkins-Tanton, L.T., 2009. Vertical mantle flow associated with a lithospheric drip beneath the Great Basin. *Nature Geoscience* 2, 439–444. doi:[10.1038/NGEO526](https://doi.org/10.1038/NGEO526).
- Xue, M., Allen, R.M., 2007. The fate of the Juan de Fuca plate: implications for a Yellowstone plume head. *Earth and Planetary Science Letters* 264, 266–276. doi:[10.1016/j.epsl.2007.09.047](https://doi.org/10.1016/j.epsl.2007.09.047).
- Zandt, G., Carrigan, C.R., 1993. Small-scale convective instability and upper mantle viscosity under California. *Science* 261, 460–463.
- Zandt, G., Gilbert, H., Owens, T.J., Ducea, M., Saleeby, J., Jones, C.H., 2004. Active foundering of a continental arc root beneath the southern Sierra Nevada in California. *Nature* 431, 41–46. doi:[10.1038/nature02847](https://doi.org/10.1038/nature02847).
- Zelt, C., 1999. Modelling strategies and model assessment for wide-angle seismic traveltimes. *Geophysical Journal International* 139 (1), 183–204.
- Zhou, Y., Nolet, G., Dahlen, F.A., Laske, G., 2006. Global upper-mantle structure from finite-frequency surface-wave tomography. *Journal of Geophysical Research* 111. doi:[10.1029/2005JB003677](https://doi.org/10.1029/2005JB003677).